

**MATERIAL CONDITION EFFECTS ON STRESS CORROSION CRACK  
INITIATION OF COLD-WORKED ALLOY 600 IN PWR PRIMARY  
WATER ENVIRONMENTS**

**Technical Milestone Report: M3LW-19OR0402037  
April 2019**

Z. Zhai, M. B. Toloczko and S. M. Bruemmer  
Pacific Northwest National Laboratory

Research Project:  
**Stress Corrosion Crack Initiation of  
Nickel-Base Alloys in LWR Environments**  
Project Manager: S. M. Bruemmer  
Pacific Northwest National Laboratory

Conducted for:  
**Office of Nuclear Energy, U.S. Department of Energy  
Light Water Reactor Sustainability Program  
Materials Aging and Degradation Pathway**  
Pathway Manager: T. M. Rosseel  
Oak Ridge National Laboratory

## Table of Contents

<b>Project Background.....</b>	<b>3</b>
<i>Objective.....</i>	<i>3</i>
<i>Approach.....</i>	<i>3</i>
<i>Focus of Current Report .....</i>	<i>3</i>
<b>Experimental Methods .....</b>	<b>5</b>
<i>Materials .....</i>	<i>5</i>
<i>Specimens and Test Methods.....</i>	<i>6</i>
<i>Unstressed Exposure Tests .....</i>	<i>6</i>
<i>SCC initiation tests .....</i>	<i>8</i>
<i>Microstructural Characterization.....</i>	<i>12</i>
<i>Examination of Unstressed Exposure Coupons.....</i>	<i>12</i>
<i>Examination of SCC Initiation Specimens.....</i>	<i>13</i>
<i>Creep Strain Measurements.....</i>	<i>14</i>
<b>Results.....</b>	<b>15</b>
<i>Characterizations of IGA and Short Crack Growth.....</i>	<i>15</i>
<i>Characterizations of SCC Initiation Morphology.....</i>	<i>27</i>
<b>Discussion.....</b>	<b>36</b>
<i>Effects of Grain Boundary Carbides on IG Oxidation and SCC Initiation .....</i>	<i>36</i>
<i>Effects of Stress on IG Oxidation and SCC Initiation .....</i>	<i>37</i>
<i>Effects of Cold Work .....</i>	<i>39</i>
<i>Implications on Model Development for SCC Initiation.....</i>	<i>40</i>
<b>Summary and Conclusions.....</b>	<b>41</b>
<b>Acknowledgement .....</b>	<b>41</b>
<b>References.....</b>	<b>42</b>

## **Project Background**

### *Objective*

This research project addresses one of the least understood aspects of stress corrosion cracking (SCC) for light-water reactor (LWR) pressure boundary components - crack initiation. The focus of the work is to investigate important material (composition, processing, microstructure, strength) and environmental (temperature, water chemistry, electrochemical potential, stress) effects on the SCC susceptibility of corrosion-resistant, nickel-base alloys. The primary objectives are to identify mechanisms controlling crack nucleation, investigate the transition from short to long crack growth in these alloys under realistic LWR conditions and help establish the framework to effectively model and mitigate SCC initiation processes.

### *Approach*

Alloy 600 materials were selected for the first phase of SCC initiation experimentation followed by testing on the more resistant Alloy 690 materials. For both alloys, material variants known to influence SCC response are being examined including cold/warm work (forged, rolled and tensile strained), banded/inhomogeneous microstructures (plate versus extruded tubing), grain boundary precipitation (heat-to-heat variations, mill-annealed, solution annealing and changes due to thermal treatments) and surface grinding (various damage depths, surface roughness and nanocrystalline layers). Materials and material conditions have been identified and obtained from an ongoing research project for the U.S. Nuclear Regulatory Commission (NRC) where stress-corrosion crack growth has been characterized, thus creating an important link between SCC initiation and propagation behavior. Detailed examinations have been performed using optical and electron microscopy to establish key bulk and surface microstructural features that may act as initiation precursors. Dedicated test systems with continuous in-situ detection of crack formation were designed and constructed enabling SCC initiation experimentation of a range of Alloy 600 and 690 materials. After SCC testing in high temperature autoclave systems, surface and near-surface characterizations were conducted to document nano-to-microscale initiation precursors leading to macroscopic stress corrosion cracks. The fundamental understanding of how the near-surface microstructure is degraded during high-temperature water exposure is essential to an improved predictive methodology for SCC initiation. Collaborations with ongoing PNNL projects supported by the NRC and EPRI play an important role in our research and has enabled testing on Alloy 600/690 and Ni-base alloy weld metals.

### *Focus of Current Report*

The main goal of this report is to document an improved mechanistic understanding of SCC initiation in Alloy 600 obtained through recent experimentation and data analysis to facilitate development of a physically-based model to predict SCC initiation behavior. Built on experience previously gained in this program and via collaboration with industry partners (NRC

and EPRI), systematic tests and data analyses have been conducted in FY19 on a selected Alloy 600 heat to evaluate the role of grain boundary (GB) carbide, applied stress, and cold work on intergranular attack (IGA), crack nucleation and short crack growth. The material has been tested in the as-received, mill-annealed condition or after subsequent solution annealing to remove carbide precipitation. A final condition evaluated was solution annealed followed by a thermal treatment to produce a semi-continuous distribution of GB carbides. SCC initiation response of these material conditions were investigated by constant load testing in simulated pressurized water reactor (PWR) primary coolant environments. With periodic examination of the specimens, morphological and dimensional evolution of precursor damage over time was carefully documented and compared to data obtained from an EPRI program in which unstressed coupons with the same material conditions were exposed to the same environment. Results reveal a predominant role played by mechanical factors where creep likely made a significant contribution in every stage leading to practical SCC initiation. Implications of test results on modeling of SCC initiation behavior of Alloy 600 is discussed and areas needing further investigation are identified.

## Experimental Methods

### Materials

As described in prior milestones reports [1-4], extensive SCC initiation testing has been performed on five different Alloy 600 heats in various cold-worked conditions. The current work has focused on one heat (NX6106XK-11) because of its high bulk carbon concentration and susceptibility to SCC initiation in the as-received mill-annealed (MA) condition. This carbon level enabled the microstructure to be effectively modified by heat treatment. The basic information and bulk composition of this heat are listed in Table 1.

Table 1. Bulk compositions (wt%, unless specified otherwise) and initial condition of Alloy 600 material investigated in this study.

Material and Heat No.	Source and Description	Composition	Heat Treatments
Alloy 600MA NX6106XK-11	Special Metals 2-inch thick plate	Ni-16.4Cr-8.5Fe-0.06C-0.23Mn-0.22Si-0.22Al-0.30Ti-0.01Cu-0.001S-0.004P-83 appm B*	927°C for 3.5 hr + WQ

\*The B content is measured by glow discharge mass spectrometry (GDMS).

To evaluate the effect of material condition and grain boundary (GB) carbides on SCC, the as-received material was first solution annealed (SA) at 1100°C for 30 minutes and water quenched (WQ) to dissolve pre-existing carbide precipitates. The SA material was then thermally treated (TT) at 704°C for 12 hours followed by air cooling to produce a semi-continuous distribution of GB carbides. Part of the SA and SA+TT materials were then cold forged (CF) to a 15% reduction in thickness to evaluate the effect of cold work on SCC initiation, which will be detailed later. Prior to all testing, SEM examinations were performed documenting a grain size varying from 100-300 µm in both materials with no IG carbides in the SA material and a semi-continuous distribution of carbides were observed at high-energy GBs in the SA+TT material (Figure 1). The carbides produced by the thermal treatment were mostly ellipsoidal in shape and 100s of nm in size. In addition, a high density of transgranular (TG) precipitates were found along with the IG precipitates. These were usually rod-shaped and crystallographically aligned with the alloy matrix. No significant crystallographic faceting was observed, suggesting the precipitates do not exhibit strong alignment with the fcc alloy matrix. Detailed scanning electron microscopy (SEM) examinations of polished surfaces were performed to assess the GB carbide coverages. The SA+TT material was estimated to have a linear carbide coverage of ~52%, while the SA material exhibited no GB carbides. It is also noteworthy that cold forging produced some permanent GB damage in the TT+15%CF specimen, including occasional small cavities at carbide-matrix interfaces and cracks inside carbides.

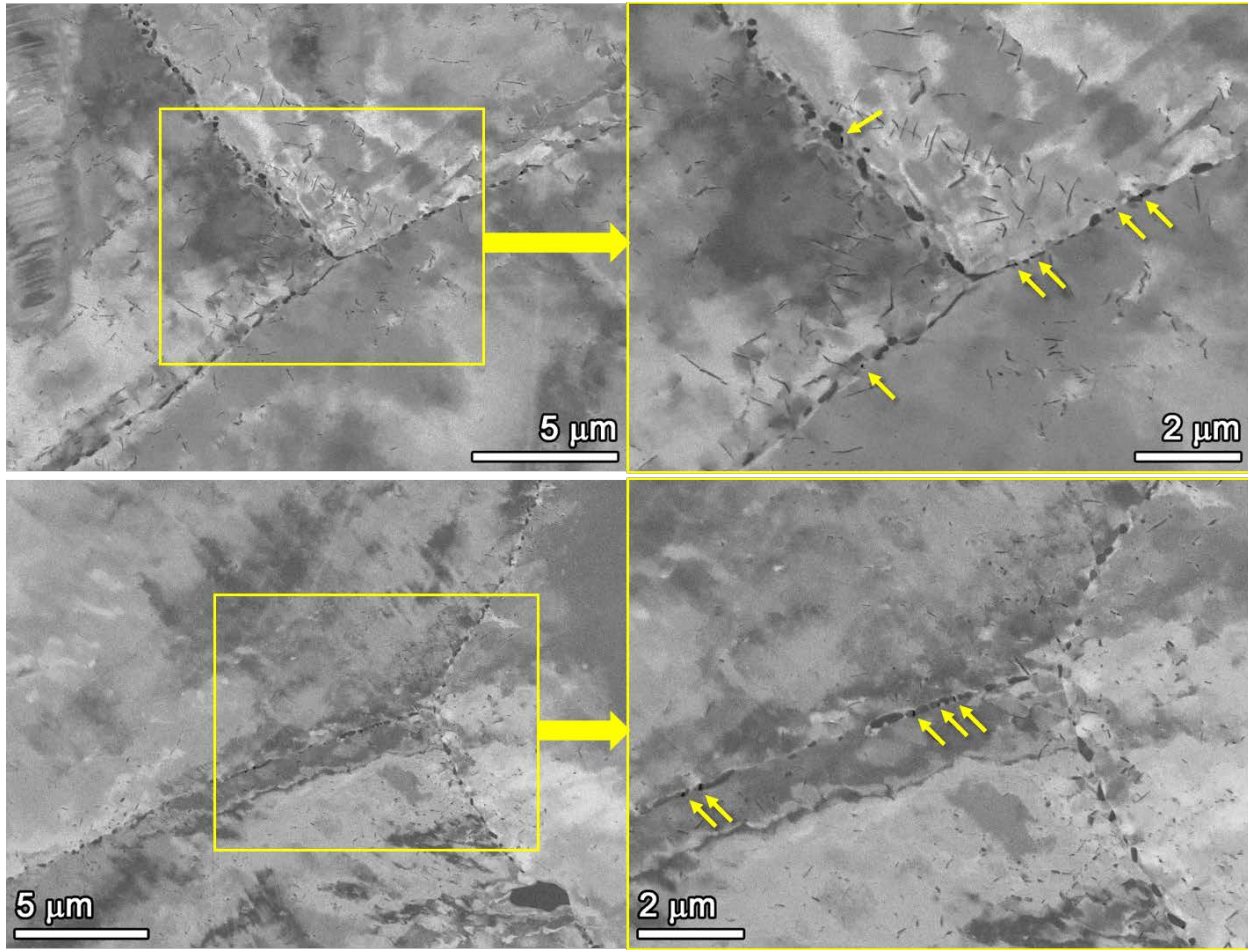


Figure 1. Representative SEM-BSE images of the GB carbides coverage of the 15%CF Alloy 600TT heat NX6106XK-11 material prior to testing. Arrowed features are cavities at carbide-matrix interface or cracks inside carbides produced by cold forging.

### *Specimens and Test Methods*

#### Unstressed Exposure Tests

Corrosion tests on unstressed specimens were conducted in simulated PWR primary water to assess material condition effects on intergranular attack (IGA) in collaboration with a recent EPRI project [5] at PNNL. Circular plate coupons prepared using electric discharge machining (EDM) with approximate dimensions of 15 mm diameter and 5 mm thickness (Figure 2A) were used for the unstressed exposure tests. All surfaces of the as-machined coupons were removed with coarse SiC paper to eliminate contaminants introduced by the EDM process (S and Cu in particular). Both flat surfaces were then polished to 600 grit SiC and one side was further polished to an electron backscatter diffraction (EBSD) quality finish with 50 nm colloidal silica. The results presented herein focus on the heat NX6106XK-11 only. Coupons were produced from each material condition in triplicate with the intention of extracting one coupon from each

material set at different exposure times (1000 h, 4400 h, and “long-term” test that is currently at 7000 h and still ongoing at the time of this report). The fully loaded coupon tree loaded into the stainless-steel autoclave is shown in Figure 2B. Coupons were suspended individually with a Pt wire wrapped in a ceramic sheath to prevent galvanic coupling. The edge of each coupon was also engraved with the sample name to confirm the material heat and thermomechanical history. A summary table of the coupons from the NX6106XK-11 heat and their exposure times are identified in Table 2.

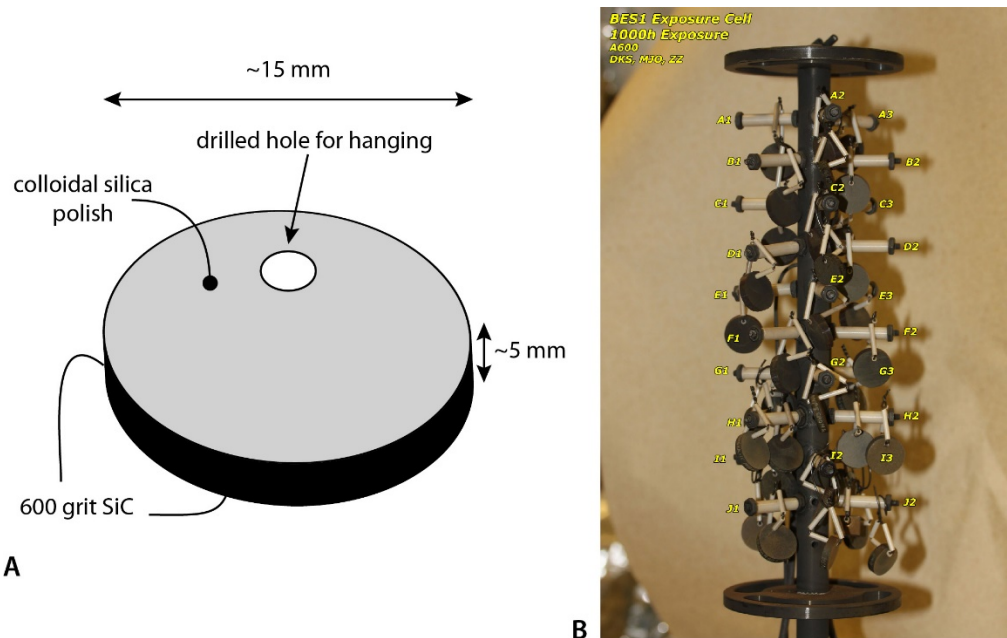


Figure 2. (A) Schematic illustration of the exposure coupon geometry and respective surface finishes. (B) Photograph of the exposure coupons on the tree mounted into the stainless autoclave. Coupons of each material condition were produced in triplicate and each coupon is suspended from the exposure tree by ceramic-encased Pt wire strung through a drilled hole in each coupon.

Table 2. Summary of Alloy 600 heat NX6106XK-11 exposure coupons. Each row corresponds to an individual coupon of the indicated material, thermomechanical history, and time exposed to 360°C simulated PWR primary water.

Thermal History	Cold Work	Time (h)
SA	0	1000
SA	0	4400
SA	0	13000+*
SA+TT	0	1000
SA+TT	0	4400
SA+TT	0	13000+
MA	15%	1000
MA	15%	4400
MA	15%	13000+
SA	15%	1000
SA	15%	4400
SA	15%	13000+
SA+TT	15%	1000
SA+TT	15%	4400
SA+TT	15%	13000+

\* Ongoing exposure as of April 2019.

The exposure water conditions were established to simulate PWR primary water chemistry (1000 ppm B and 2 ppm LiOH). The pressurized water temperature was maintained at 360°C to facilitate accelerated testing of the IG corrosion/oxidation response. The electrochemical potential was set at the Ni/NiO line using a dissolved concentration of 25 cc H<sub>2</sub> / kg H<sub>2</sub>O where IGA/SCC susceptibility is expected to be maximized. At each target exposure time, the autoclave was cooled and drained then one coupon from each material condition was extracted, rinsed and dried for destructive examinations. The remaining coupons were returned to the autoclave to resume exposure to longer times.

### SCC initiation tests

Uniaxial tensile specimens for SCC initiation tests were machined with the gauge section along the thickness direction (short transverse) of the plate. The dimensions of the specimen are provided in Figure 3. The gauge length for all specimens is identical (4 mm), but the diameter varies so that different applied stress can be achieved when specimens are loaded in the same string. This relatively small specimen size was selected for multi-specimen testing and has the advantage of reducing the magnitude of creep contribution to the direct current potential drop (DCPD) signal, thus making DCPD more sensitive to changes in cross-sectional area due to cracking. It also enables full characterization of the gauge surface by SEM in a reasonable period of time. Prior to loading up in the autoclave, all specimens were polished to a 1 µm finish. This surface preparation removes near-surface mechanical damage and allows detailed

assessment of precursor damage on the surface. Details of the surface preparation process have been reported previously [2].

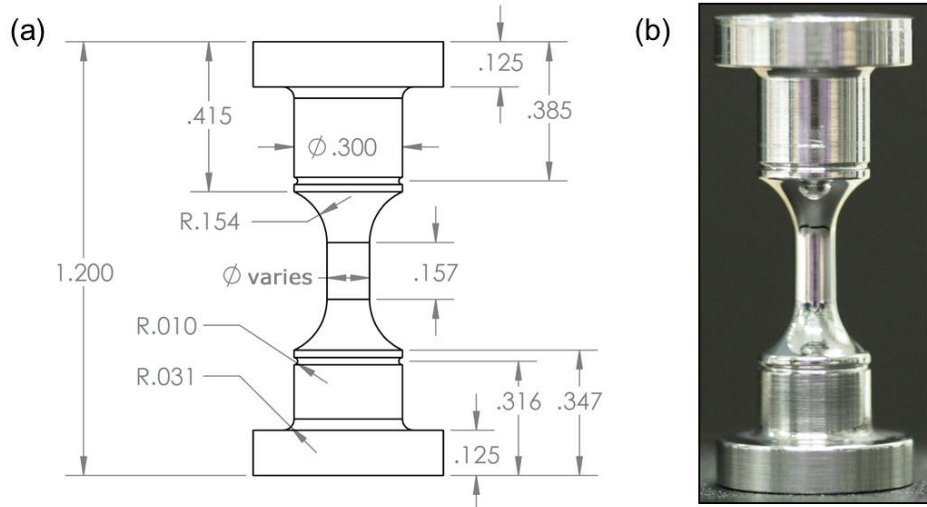


Figure 3. PNNL initiation specimen design. Gauge diameter is selected based on material strength and can be varied from 2.75-4.5 mm and the gauge length is 4.0 mm. Overall height is 30.5 mm (1.2 inches).

A six-specimen autoclave equipped with active load control and in-situ detection of crack initiation by the DCPD technique was used for this study. Figure 4 shows the load train and DCPD instrumentation for the typical SCC initiation specimen set up at PNNL. The tests were conducted in an environment that simulates the PWR primary water (1000 ppm B, 2 ppm Li) at 360°C and 20.4 MPa with a dissolved hydrogen content of 25 cc/kg to maintain a corrosion potential at the Ni/NiO stability line. In this study, the autoclave was first used to test six specimens in the TT+15% CF condition followed by six specimens in the SA+15% CF condition. The initial material and loading condition of all specimens are listed in Table 3. All specimens were tested at or just slightly above their as-prepared yield stress under constant load. Full load was applied to the specimens within 1-2 days of reaching full temperature enabling specimens to be pre-oxidized before loading. At the start of a test, the target load (the load at ~0.2% plastic strain) was achieved over a period of ~1 hour at a constant strain rate of  $\sim 10^{-5}/\text{s}$ . This rate was chosen to load specimens to their yield stress sufficiently fast to reduce the risk for SCC formation during the initial loading. It also allows DCPD to monitor the stress-strain evolution with a sufficiently low noise level during this loading step. As shown in Figure 5, individual specimens would sometimes yield slightly earlier than the others in a multi-specimen load train system due to intrinsic difference in yield strength and/or gauge diameter. In this case, small amounts of plastic strain up to  $\sim 1.5\%$  were allowed in order to achieve yield in the other specimens. The specimens were then held at actively controlled constant load until crack initiation. All relevant environmental parameters and DCPD data were monitored and continuously written to a file. For this study, test interruptions were planned at  $\sim 480$  hours and  $\sim 1000$  hours to document surface damage morphology evolution in all specimens. One

specimen was also removed at each test interruption from both the TT+15%CF and SA+15%CF material for destructive examination of precursor damage. In addition, selected specimens were removed from the test if SCC initiation was detected by DCPD. In such cases, the remaining specimens would be taken back to their original load via monitoring stress versus strain response upon restart of the test. Figure 6 shows the evolution of both non-referenced and referenced strains throughout exposure of an Alloy 600 specimen. By subtracting the DCPD reference voltage from the gauge voltage, the contribution of resistivity drift is eliminated in the referenced strain response. While creep and cracking are both likely to be simultaneously contributing to the measured response, the SCC initiation time is determined as any obvious increase in strain rate occurs for both non-referenced and referenced strains, which will be shown later.

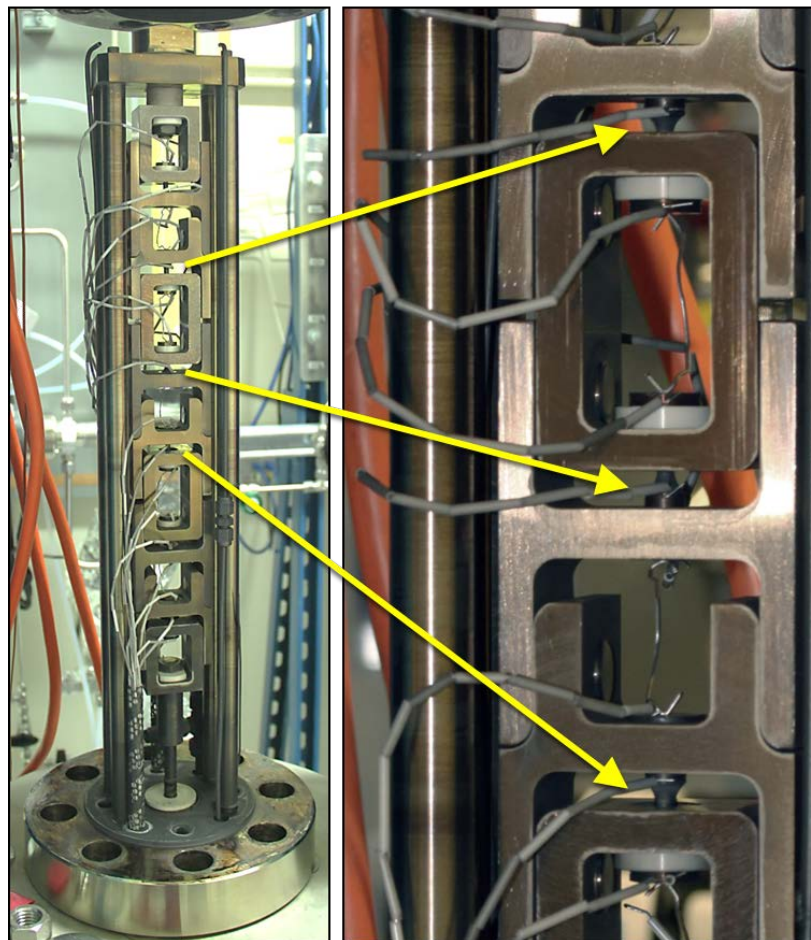


Figure 4. Crack initiation test system load train at PNNL in the small SCC initiation test system with capacity of testing up to 6 fully instrumented specimens.

Table 3. Summary of specimen test conditions of the Alloy 600 plate heat NX6106XK-11.

Spec. ID	Material Condition	Surface Finish	Applied Stress (MPa)
IN273	TT + 15% CF	1 $\mu\text{m}$	533
IN274	TT + 15% CF	1 $\mu\text{m}$	533
IN275	TT + 15% CF	1 $\mu\text{m}$	530
IN276	TT + 15% CF	1 $\mu\text{m}$	532
IN277	TT + 15% CF	1 $\mu\text{m}$	532
IN278	TT + 15% CF	1 $\mu\text{m}$	530
IN282	SA + 15% CF	1 $\mu\text{m}$	466
IN283	SA + 15% CF	1 $\mu\text{m}$	467
IN284	SA + 15% CF	1 $\mu\text{m}$	467
IN285	SA + 15% CF	1 $\mu\text{m}$	468
IN286	SA + 15% CF	1 $\mu\text{m}$	467
IN287	SA + 15% CF	1 $\mu\text{m}$	473

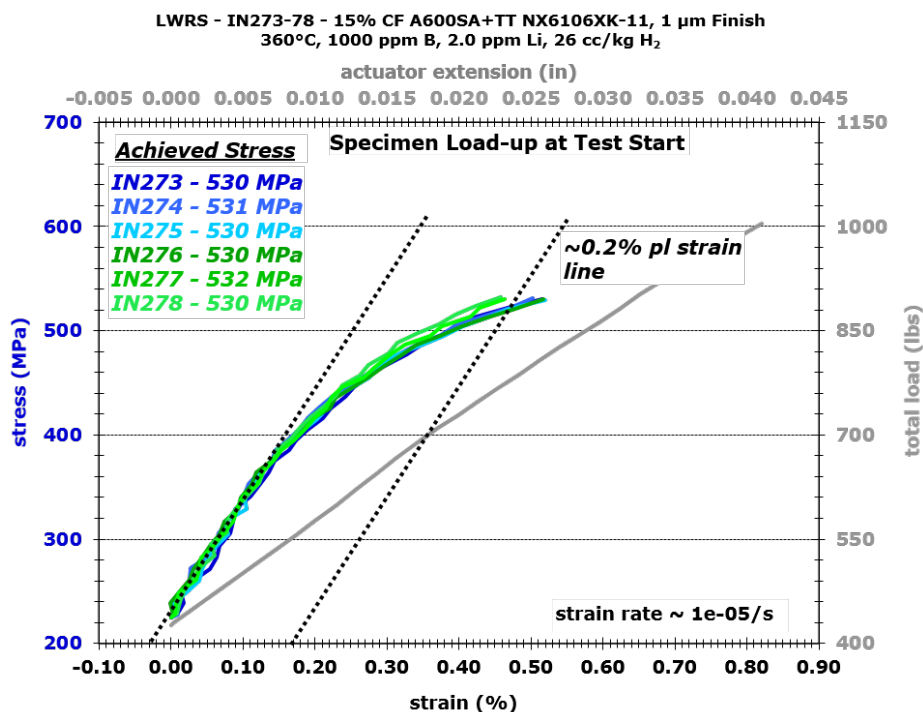


Figure 5. Example of stress versus strain plot during initial loading of tensile specimens for SCC initiation testing. The actuator displacement and the total load is plotted in the secondary x (upper) and y (right) axis, respectively.

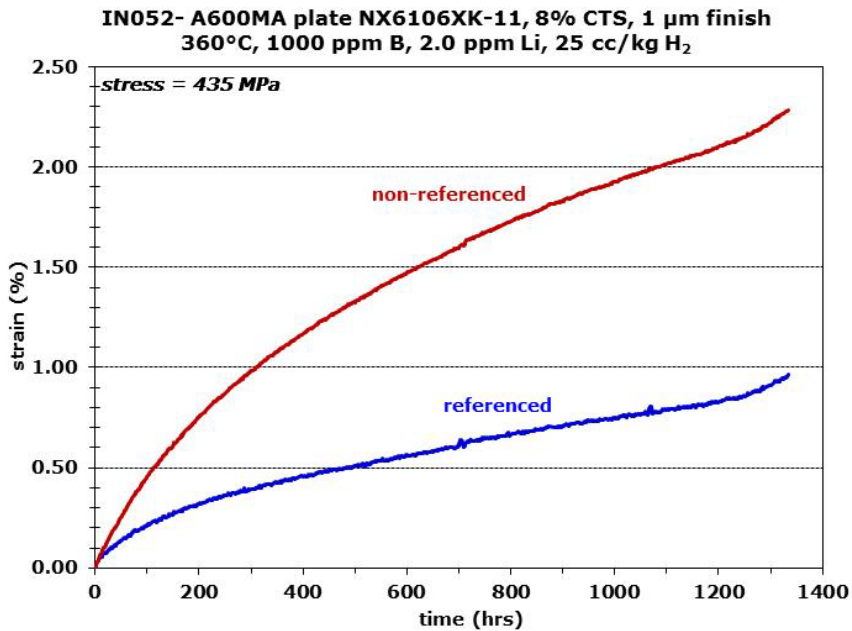


Figure 6. Non-referenced and referenced DCPD strain response for IN052, a 8%CTS specimen from Alloy 600MA heat NX6106XK-11.

#### *Microstructural Characterization*

The microstructural characterizations focus mainly on acquiring morphological and quantitative information of IGA and cracks for further analyses. Most examination was performed using a JEOL 7600 SEM in the backscatter electron (BSE) mode. The characterization procedure for each test will be detailed in the following sections. Supplementary high-resolution characterizations by transmission electron microscopy (TEM) and atom probe tomography (APT) were also performed on a subset of the specimens as part of the collaborative EPRI project. These exams were conducted to better understand the IG corrosion/oxidation behavior as a function of GB chemistry and are reported elsewhere [6].

#### Examination of Unstressed Exposure Coupons

The exposure coupons taken out at each test interruption were cut in half using EDM. One half of each coupon was mounted into epoxy and mechanically polished to a “mirror finish” using colloidal silica for SEM examinations in cross-section. It is critical to ensure that the edge of the cross-sections do not curve during mechanical polish, otherwise it may be difficult to obtain reliable measurements of the IGA depth (usually only a few micrometers deep or below) located on these edges. To accomplish this, the cross-sectioned coupons were clamped between two metal fixture plates like a sandwich using spacers. The whole set was then mounted into epoxy. The material of the plate had a similar hardness as the test coupons so that material was removed evenly during polishing to provide a sufficiently flat edge for reliable IGA depth measurement.

The other half was left unmounted to enable more facile preparation of TEM and APT specimens as needed.

Low voltage was used during SEM imaging to reveal detailed compositional contrast of the IGA. For each examined coupon, the IGA depth measurements were performed on at least 50, as many as 120, neighboring high-energy GBs. This provides a representative sample size for statistical analysis. In addition, the IGA morphology at some GBs were documented at higher magnifications enabling comparisons between material conditions and exposure times.

#### Examination of SCC Initiation Specimens

Surface SEM examinations were performed on all SCC initiation specimens at planned test interruptions and after DCPD detection of crack initiation, enabling the evolution of crack morphology to be evaluated as a function of exposure time. Oxford Aztec software was used to automate stage movement such that the entire gauge surface could quickly be mapped and montages created. In order to achieve this, four fiducial scribe marks ( $90^{\circ}$  to one another) were made at the button ends of each specimen to keep track of the specimen orientation. Each of the four orientations was then mapped using high-keV BSE montage imaging so that features covered by thin surface oxides can be revealed. As shown in Figure 7, the surface of the entire gauge section and most of the fillet region of the specimens was examined on each rotation.

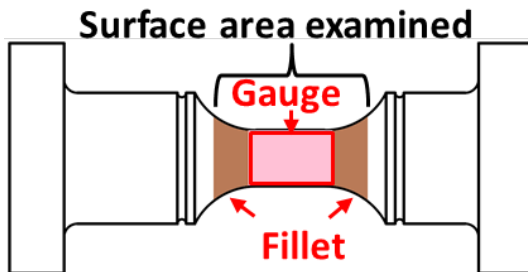


Figure 7. Schematic of the gauge and fillet surface areas mapped during one rotation in the SEM during examinations.

In addition, one specimen was removed and cross-sectioned at each test interruption using the same procedure described for the unstressed exposure coupons. One half of the specimen was then mounted into epoxy and polished to a colloidal silica finish for SEM examination in cross-section. Similarly, 50-120 high-energy GBs were measured for the depth of IGA/short cracks and morphology documented for some.

### Creep Strain Measurements

In the attempt to better quantify creep strain induced during exposure to PWR primary water, the gauge length and diameter of the specimens were measured prior to the test and after each test interruption. Since the edge of the actual gauge is difficult to define as it gradually links to the wider shoulder through a smooth fillet, the gauge length was actually measured between the grooves located on the left and right side of the fillet regions shown in Figure 7. In order to reduce measurement error, 3-4 measurements were carried out for each dimension. The averaged creep strains were then calculated using equations below:

$$\text{Uniaxial creep strain based on gauge length: } \varepsilon_{\text{cr},L} = \frac{L-L_0}{L_0} - \varepsilon_p$$

$$\text{Uniaxial creep strain based on gauge diameter: } \varepsilon_{\text{cr},D} = -\frac{D-D_0}{\nu_{\text{cr}} D_0} - \varepsilon_p$$

where  $\varepsilon_p$  is the total amount of plastic strain accumulated during the loading processes to the yield stress as monitored using DCPD. It was later determined that the gauge diameter cannot be satisfactorily measured for all specimens due to growth of the surface oxide, making identification of the actual surface challenging. As a result, only the creep strain based on gauge length was used in further analysis.

## Results

### *Characterizations of IGA and Short Crack Growth*

As indicated in the previous section, SEM examinations were performed on the unstressed coupons exposed for 1000 and 4400 hours in 360°C PWR primary water. Representative examples of IGA in both non-CW and 15% CF unstressed coupons in the SA and TT conditions after 1000 hours of exposure are shown in Figures 8-11. For each material condition, similar IGA morphology was observed in the specimens exposed for 4400 hours. All images were collected from cross-sections of the epoxy-mounted half of the exposure coupons using low-kV BSE mode to reveal detailed compositional contrast. To facilitate comparison, the images are shown at the same or similar magnifications. In the SA condition, an interesting trend is revealed that the IGAs are generally sharper in the non-CW SA specimen in comparison to the CW counterpart. As shown in Figure 8, the oxidation penetration is confined tightly along the GB plane in the non-CW SA specimen, whereas thicker oxides were observed to extend into the surrounding grains in the 15% CF specimen (Figure 9). However, a similar trend was not observed in the non-CW and 15% CF TT specimens as oxidation trajectory deflected around the periphery of GB carbides, resulting in thicker IGAs in both specimens (Figures 10 and 11). It should be noted that most carbide/oxide interfaces exhibit a distinct bright contrast indicating a higher average density material, which has been correlated to Ni enrichment by high-resolution TEM and APT studies [6]. In addition, both the SA and SA+TT oxides exhibit varying gray-level contrast within the oxide, indicating multiple oxide phases. Generally, the darker contrast oxide can be correlated with Cr<sub>2</sub>O<sub>3</sub>.

Quantification has been performed on the IGAs in each material condition after 1000 hours of exposure in 360°C PWR primary water. This was accomplished by manually measuring the IGA depths using the ruler tool equipped in the JEOL 7600 SEM during specimen examination. For each specimen, ~100 neighboring GBs were measured to ensure statistical representativeness. The result is plotted graphically in Figure 12. The non-CW and CW pairs from each material condition are grouped with the non-CW data plotted in black and the 15%CF ones in red. The data obtained in the as-received MA condition was also shown beside those in the SA and TT conditions. The averaged IGA depth in all material conditions only varies slightly from ~1 and 2 μm. Larger variance was found within each material condition between individual GBs. For example, the non-CW TT specimen showed a variance between 800 nm and 5 μm for its IGA depth. Interestingly, the mean IGA depths are consistently deeper in the non-CW specimen in either the SA, TT or MA condition. There is also a slight tendency for the TT condition to exhibit a deeper IGA than their SA and MA counterparts. However, the differences are small and are difficult to separate from statistical error.

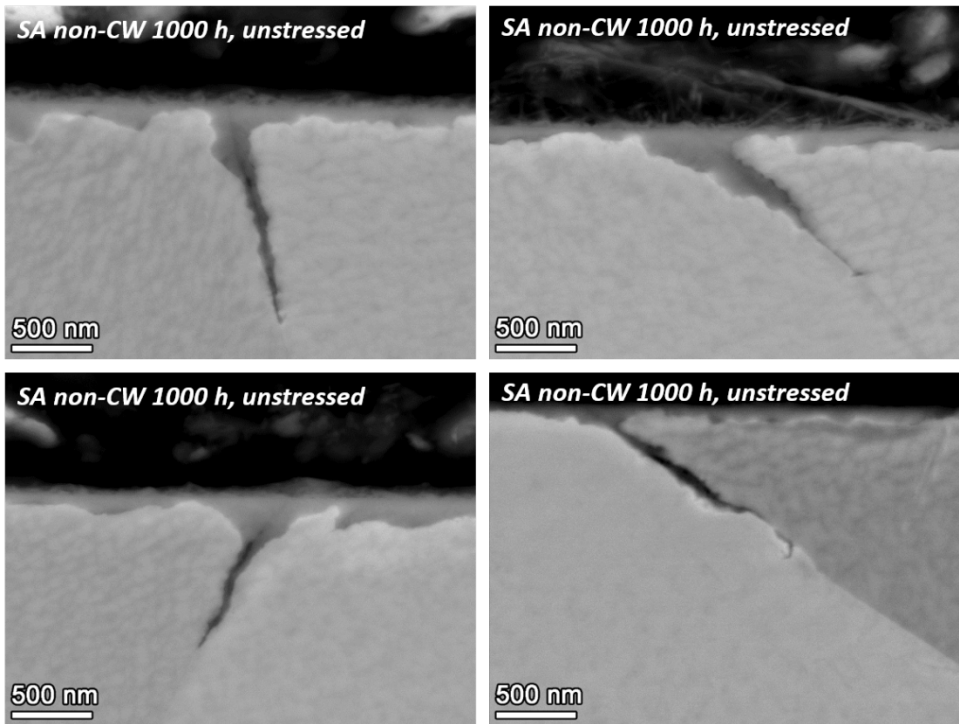


Figure 8. SEM-BSE images of representative IGA observed in the non-CW Alloy 600SA exposure coupon after 1000 hours of exposure in 360°C PWR primary water.

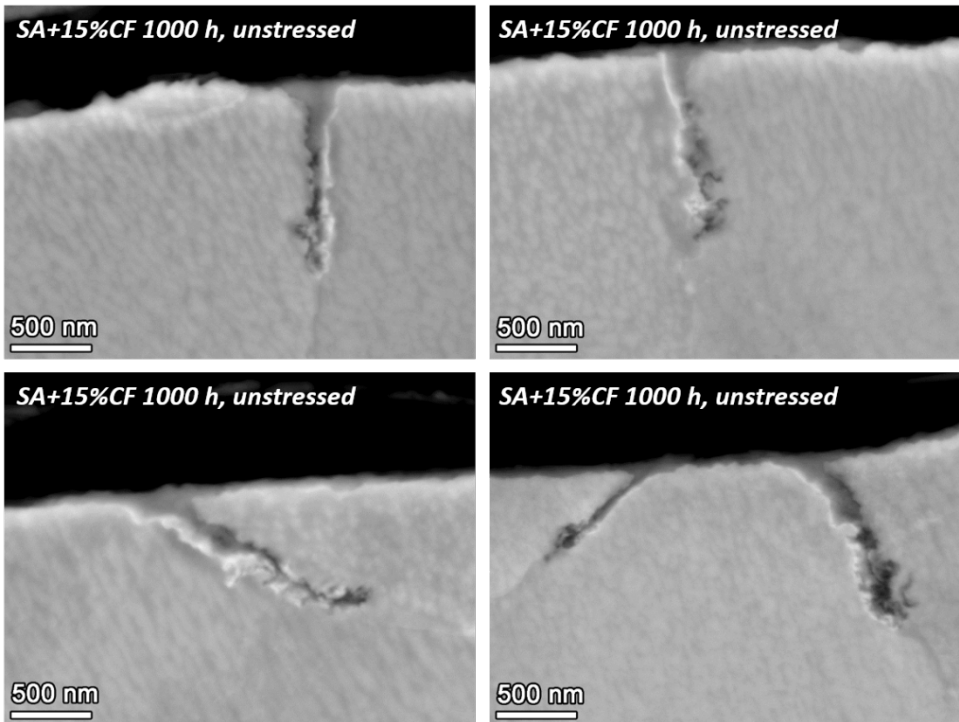


Figure 9. SEM-BSE images of representative IGA observed in the 15%CF Alloy 600SA exposure coupon after 1000 hours of exposure in 360°C PWR primary water.

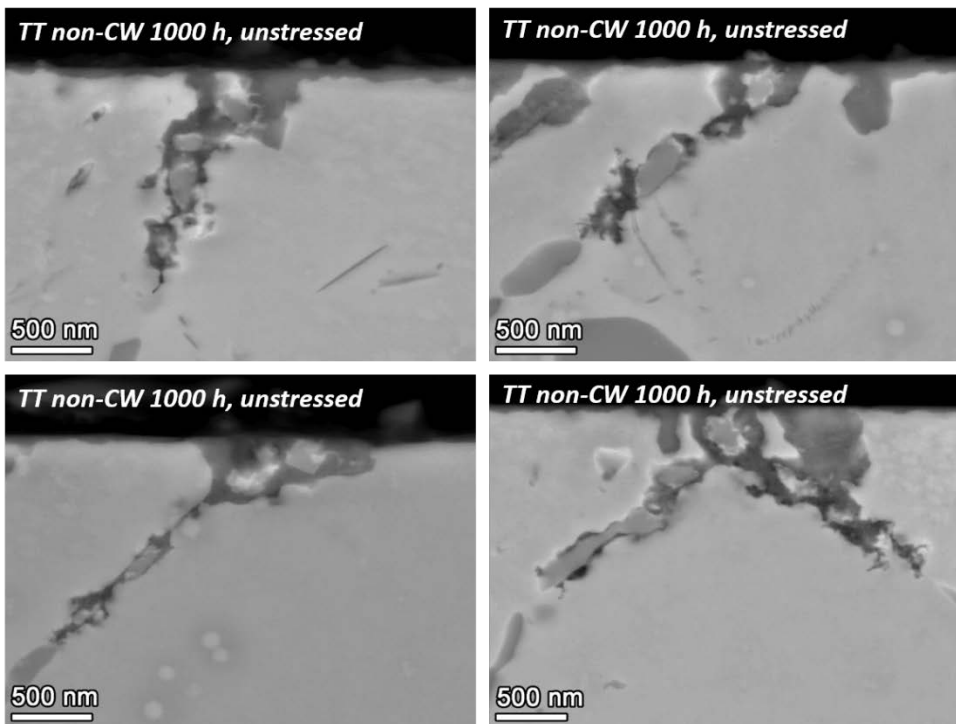


Figure 10. SEM-BSE images of representative IGA observed in the non-CW Alloy 600TT exposure coupon after 1000 hours of exposure in 360°C PWR primary water.

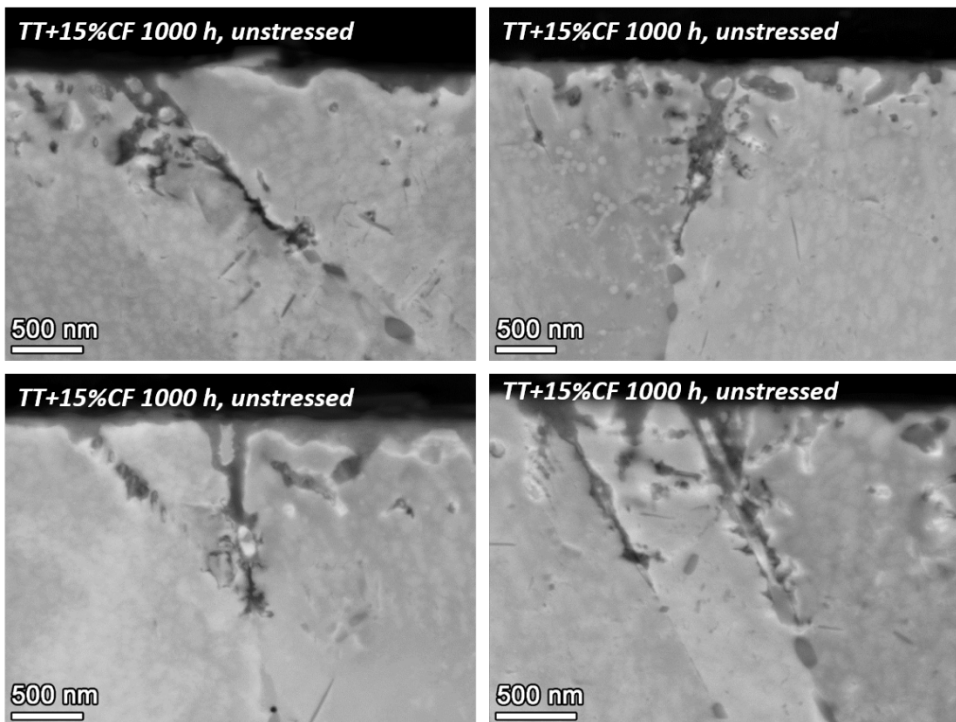


Figure 11. SEM-BSE images of representative IGA observed in the 15%CF Alloy 600TT exposure coupon after 1000 hours of exposure in 360°C PWR primary water.

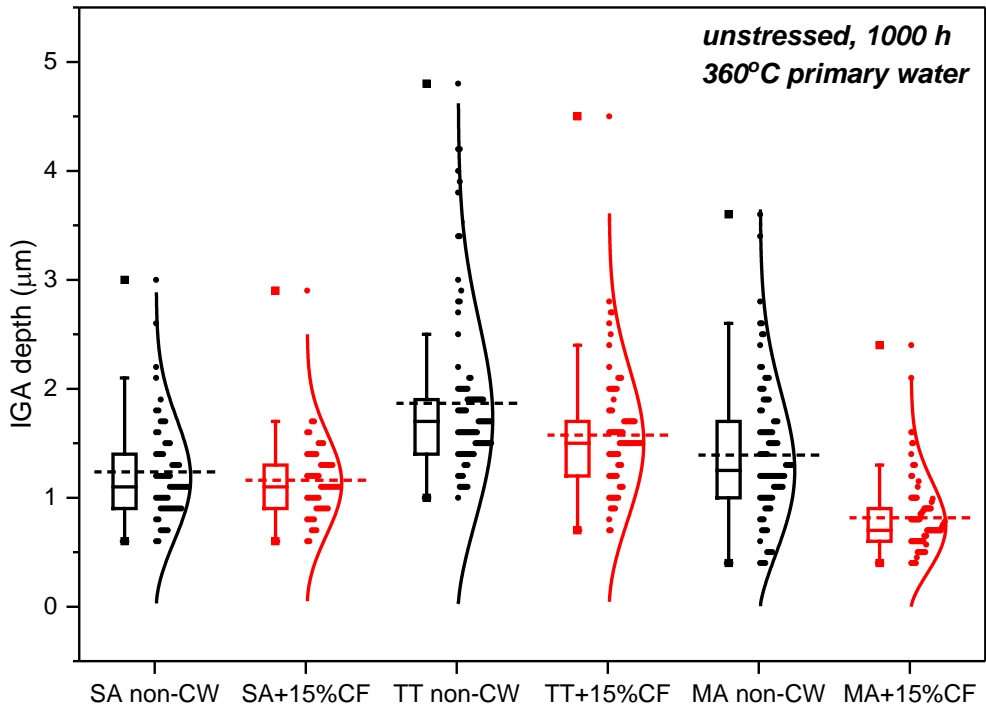


Figure 12. Summary of the measured IGA depths for the Alloy 600 heat NX6106XK-11 coupons in SA, TT and MA conditions with and without cold work after 1000 h exposure in 360°C simulated PWR primary water. Individual GB measurements are shown by symbols and the statistical distribution is shown by the box and whisker plot. The box represents the inner two quartiles of the distribution and the central line represents the median value. The dashed line represents the mean value and the curve represents the Gumbel distribution fit of the data.

Examinations of precursor damage were also performed on the SA+ and TT+15%CF SCC initiation specimens after test interruptions and at the conclusion of the test. The precursor damage in these samples can be categorized into three types: uncracked IGA, cracked IGA and short cracks. Examples of these three features are shown in Figures 13-16 for the SA+15%CF specimens and in Figures 17-21 for the TT+15%CF specimens. Most IGA in the SA+15%CF material exhibit depths of 1-2  $\mu\text{m}$  after ~480 hours of exposure (Figure 13), and some reached >5  $\mu\text{m}$  after 1000 hours (Figure 15). As compared to the unstressed coupons (Figures 8-9), the stress-assisted IGA in the initiation specimens appear to be more tightly confined along GBs. Less area with bright contrast was observed along the oxide indicating lower degree of Cr depletion. Instead, a portion of some IGA exhibit a darker contrast, suggesting that the oxide was cracked. As shown in Figures 14 and 15, a darker contrast in some IGA was found to emanate from the surface, runs down along the oxide/metal interface and ends in what appears to be lighter colored  $\text{Cr}_2\text{O}_3$  oxides. The decohered portion in this type of cracked IGA usually extends beyond 1  $\mu\text{m}$ , but no more than 2  $\mu\text{m}$ . Meanwhile, short open cracks were also observed in the specimens. As shown in Figure 16, some of these cracks were only ~1  $\mu\text{m}$  deep. It is also worth noting that the depth of some uncracked IGA are longer than the short cracks, indicating boundary-to-boundary variability in SCC initiation susceptibility.

**SA+15%CF 483 h, 466 MPa**

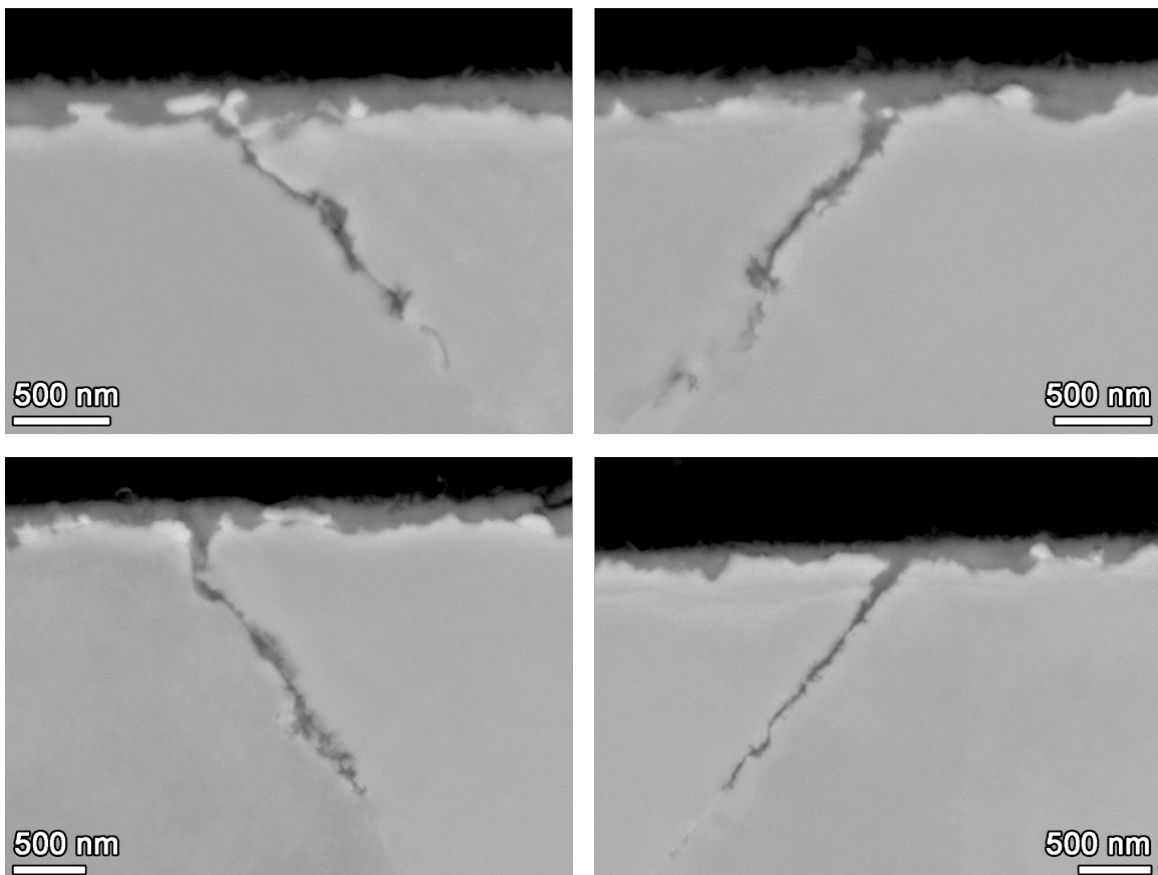


Figure 13. SEM-BSE images of representative IGA observed in the SA + 15%CF SCC initiation specimen IN282 after 483 hours of exposure loaded at yield stress in PWR primary water.

**SA+15%CF 483 h, 466 MPa**

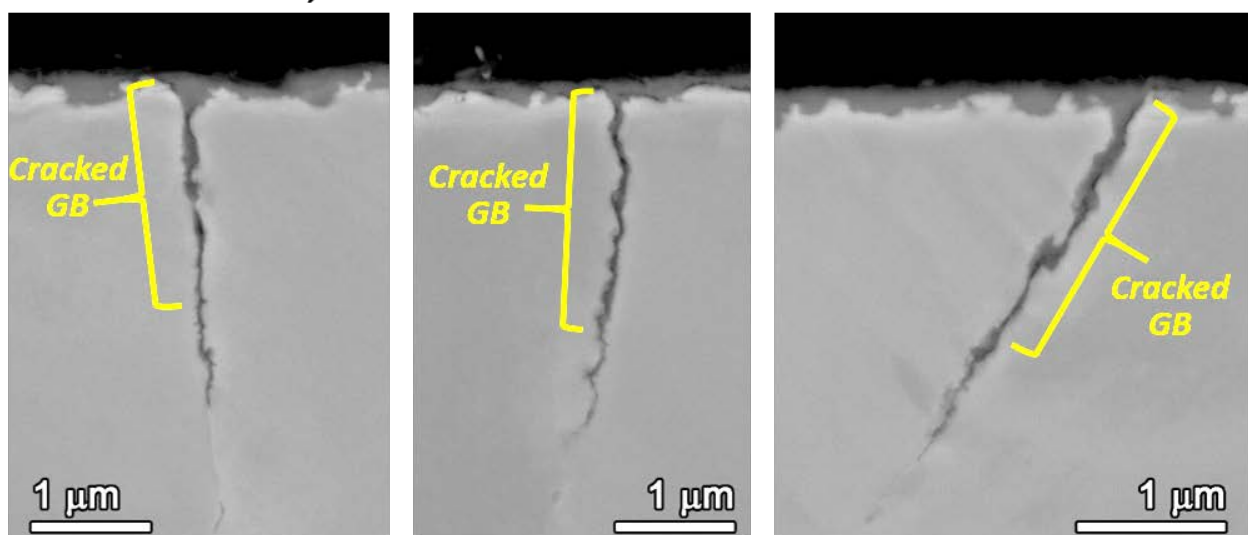


Figure 14. SEM-BSE images of cracks ending in IGA in the SA + 15%CF initiation specimen IN282 after 483 hours of exposure in PWR primary water. The cracked portions are highlighted.

**SA+15%CF 1004 h, 467 MPa**

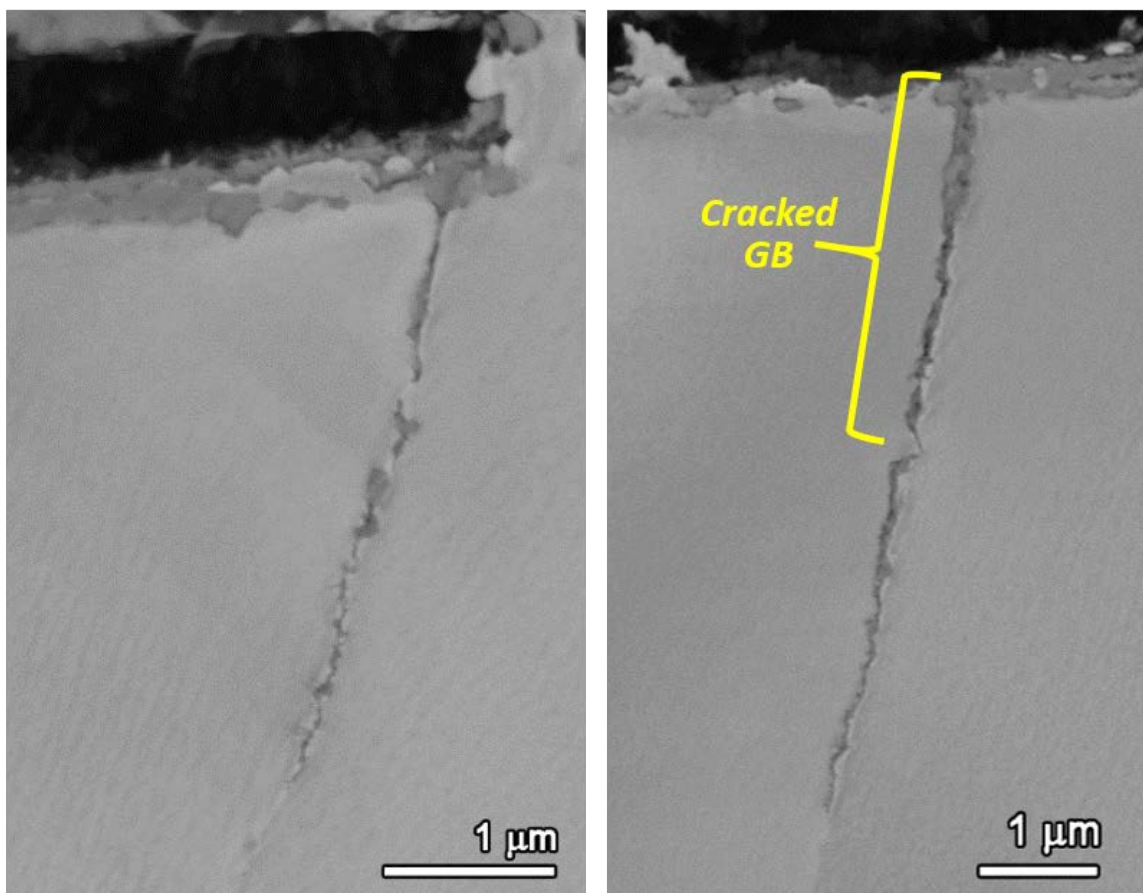
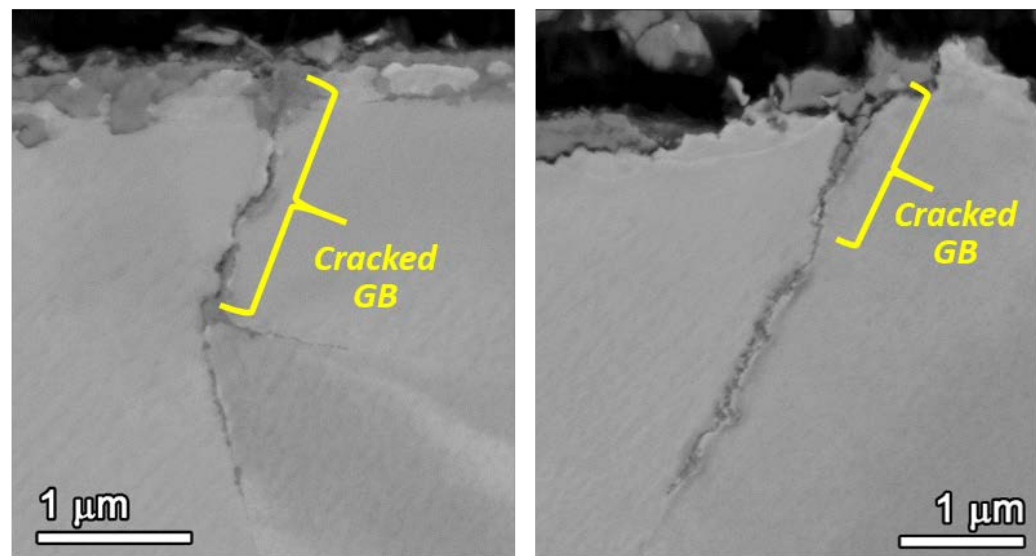


Figure 15. SEM-BSE images of uncracked and cracked IGAs observed in the 15%CF Alloy 600SA SCC initiation specimen IN284 after 1004 hours of exposure loaded at yield stress in PWR primary water. The cracked portion of the GBs are highlighted.

**SA+15%CF 1004 h, 467 MPa**

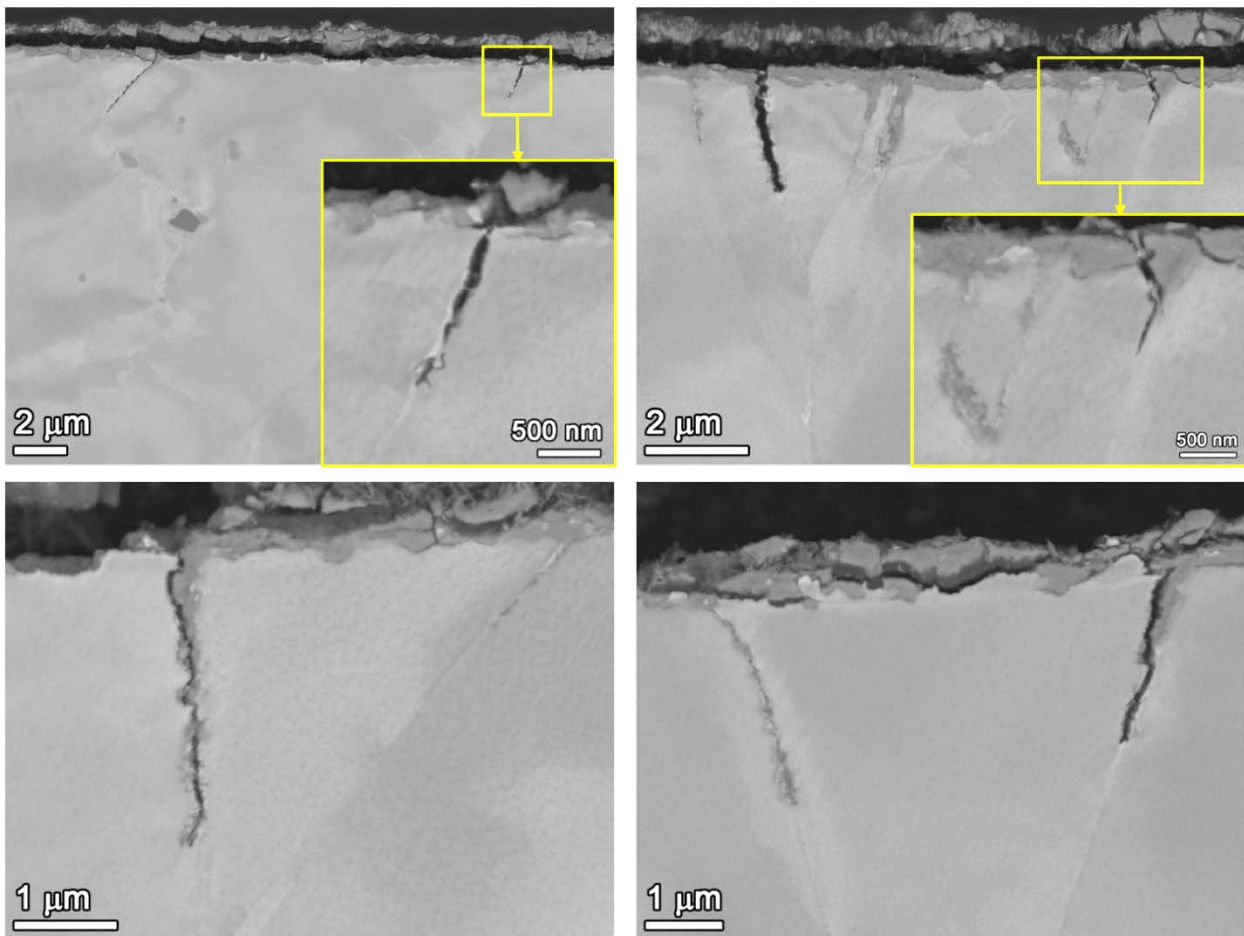


Figure 16. SEM-BSE images of IGAs and short IG cracks observed in the 15%CF Alloy 600SA SCC initiation specimen IN284 after 1004 hours of exposure in PWR primary water.

Uncracked IGA, cracked IGA and short IG cracks were also observed in the TT+15%CF Alloy 600 SCC initiation specimens after ~480 and ~1000 hours of exposure in 360°C PWR primary water. The uncracked IGAs in the SCC initiation specimens exhibit similar morphology as those observed in the unstressed TT+15%CF coupon, but shows obvious growth over time. While IGA less than 1 μm deep can be found at ~480 hours (Figure 17), the IGA observed after ~1000 hours of exposure generally exceed a depth of 2 μm (Figure 19). As shown in Figures 18 and 20, cracking along GB were also observed in many IGA reaching over 2 μm deep. In addition, fully opened, longer IG cracks extending up to ~7 μm deep are occasionally present in the specimen after 1000 hours of exposure (Figure 21).

**TT+15%CF 473 h, 530 MPa**

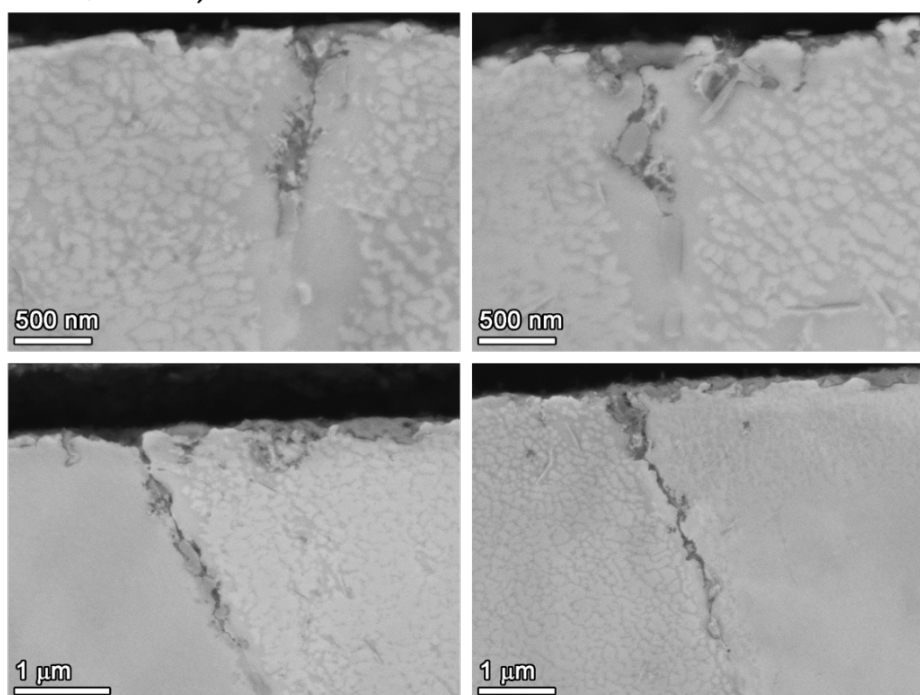


Figure 17. SEM-BSE images of representative IGA observed in the 15%CF Alloy 600TT SCC initiation specimen IN278 after 473 hours of exposure in 360°C PWR primary water.

**TT+15%CF 473 h, 530 MPa**

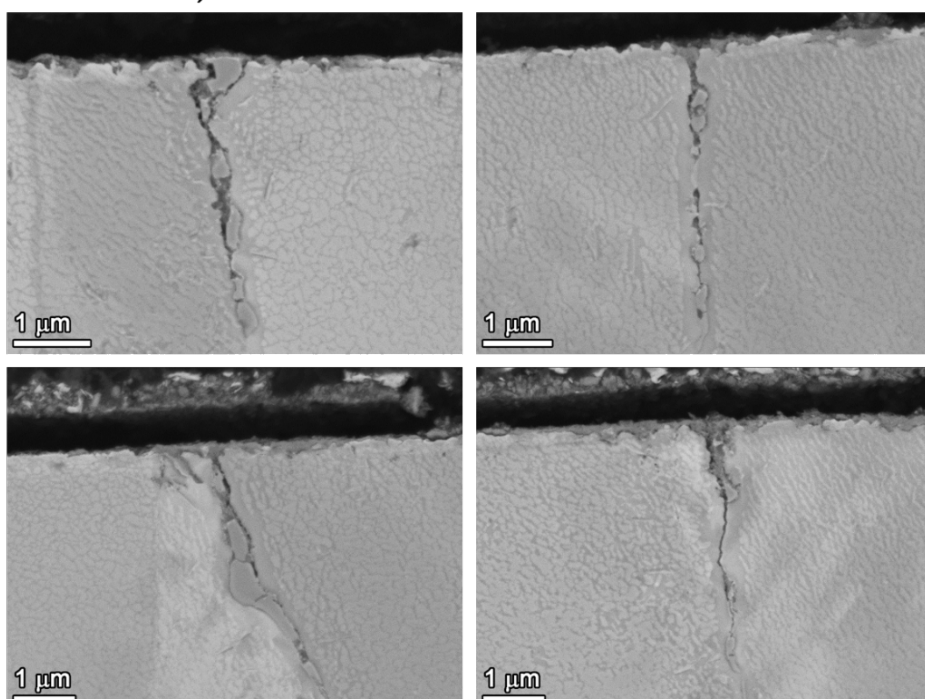


Figure 18. SEM-BSE images of representative short IG cracks observed in the 15%CF Alloy 600TT SCC initiation specimen IN278 after 473 hours of exposure in PWR primary water.

**TT+15%CF 1078 h, 532 MPa**

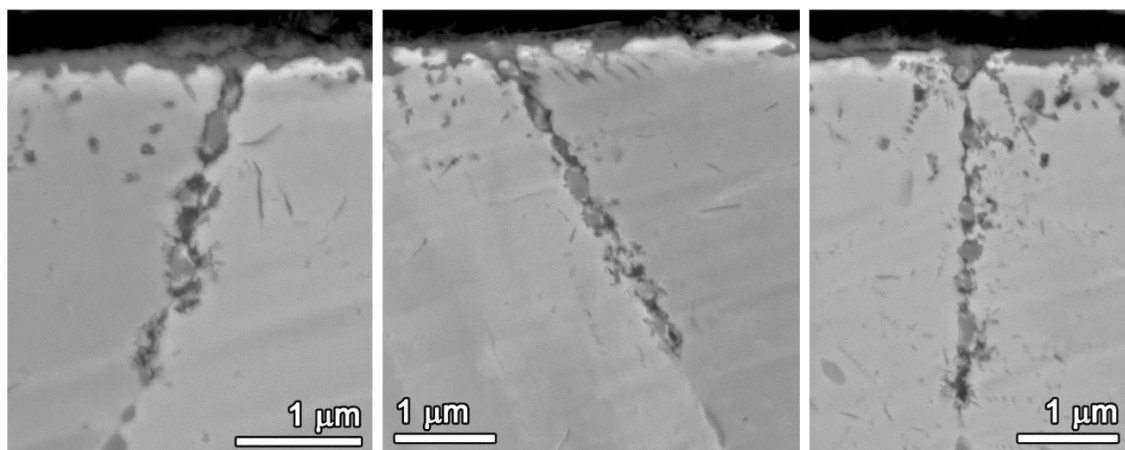


Figure 19. SEM-BSE images of representative IGAs observed in the 15%CF Alloy 600TT SCC initiation specimen IN276 after 1078 hours of exposure in 360°C PWR primary water.

**TT+15%CF 1078 h, 532 MPa**

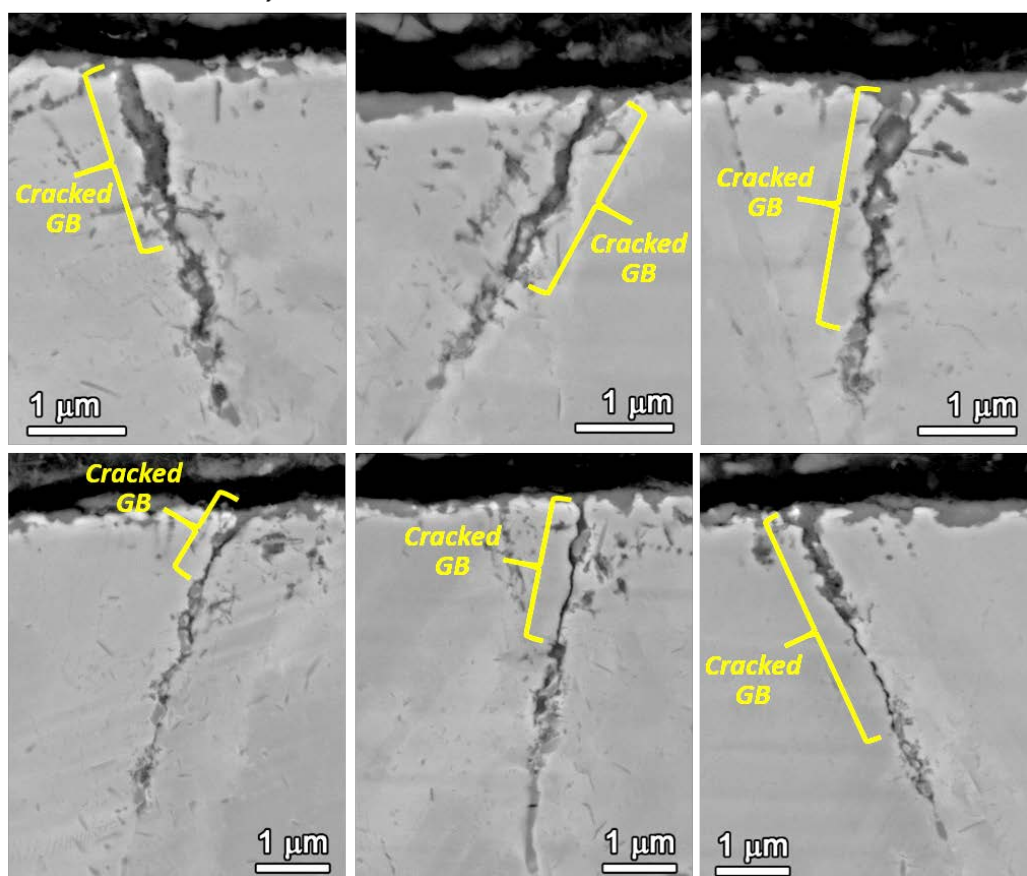


Figure 20. SEM-BSE images of short cracks ending in IGA observed in the 15%CF Alloy 600TT SCC initiation specimen IN276 after 1078 hours of exposure loaded at yield stress in 360°C PWR primary water. The cracked portion of the GBs are highlighted in the images.

**TT+15%CF 1078 h, 532 MPa**

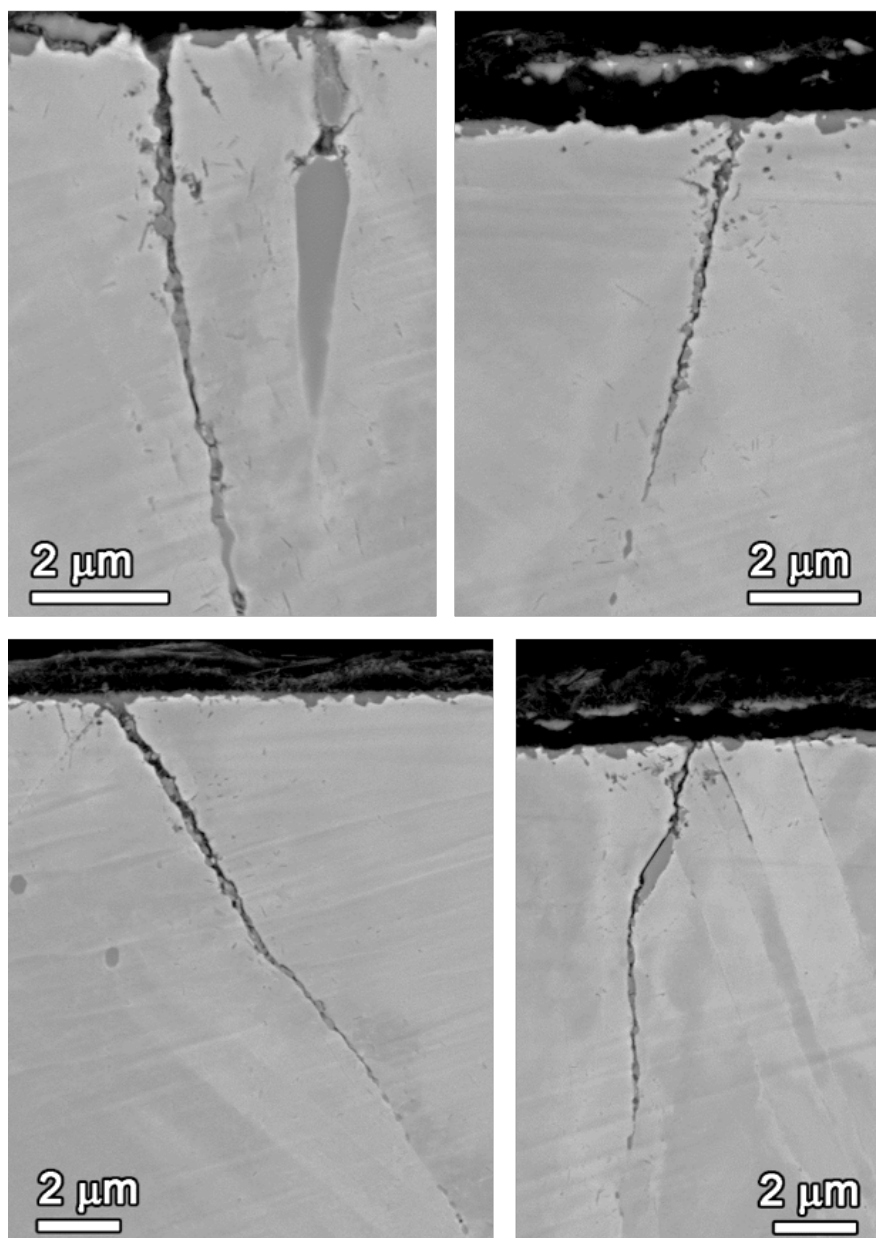


Figure 21. SEM-BSE images of representative short IG cracks observed in the 15%CF Alloy 600TT SCC initiation specimen IN276 after 1078 hours of exposure in PWR primary water.

The IGA depth distribution was also compared quantitatively between the unstressed exposure coupons and the SCC initiation specimens tested at the material yield stress. An overview is provided in Figure 22 with the time evolution shown for both types of specimens. It should be noted that cracked IGA and short IG cracks shorter than 7  $\mu\text{m}$  were observed in all the SCC initiation specimens and are included in the statistics. The average IGA depth in both the unstressed SA and TT coupons reached  $\sim$ 1-1.5  $\mu\text{m}$  after 1000 hours and exhibit little growth over extended exposure up to 4400 hours. In comparison, the average IGA depths in the SCC initiation specimens loaded at yield stress reached similar or higher values around  $\sim$ 480 hours of exposure, and continued to grow with a slowly decreasing yet obvious rate. By  $\sim$ 1000 hours, the averaged IGA depths in the initiation specimens became  $\sim$ 2 times longer than those in the unstressed coupons exposed for similar duration. More detailed IGA depth distributions in the SA+ 15%CF and TT+15%CF specimens, both stressed and unstressed, are shown in Figure 23 with the box and whisker plots. The median IGA depths exhibit a similar trend as the averaged IGA depths in Figure 22, suggesting an important role of applied stress in IGA growth.

Quantification was also performed to assess the percentage of cracked GBs in the SCC initiation specimens with results summarized in Figure 24. It is interesting to note that the SA+15%CF specimens exhibit a much higher density of short IG cracks in comparison to the TT+15%CF specimens. After  $\sim$ 480 hours of exposure,  $\sim$ 10% of all the observed high energy GBs in the SA+15%CF specimen contain short IG cracks, and this value has more than tripled after 1000 hours of exposure. Meanwhile, the percentage of cracked GBs underwent a slower growth from  $\sim$ 4% to 17% in the TT+15%CF specimens, which are less than half of the values in the SA+15%CF counterpart after comparable test durations.

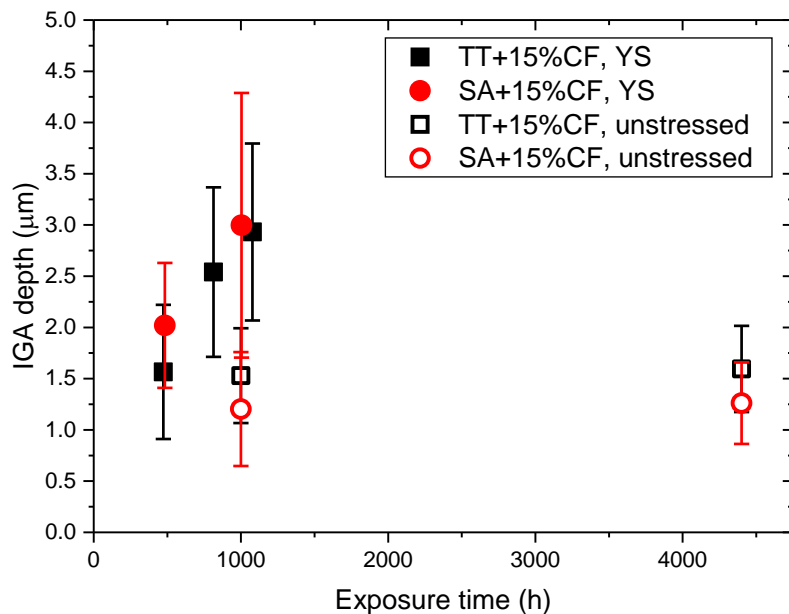


Figure 22. Summary of the time evolution of average IGA depth in the Alloy 600SA and TT unstressed exposure coupons and SCC initiation specimens loaded at yield stress.

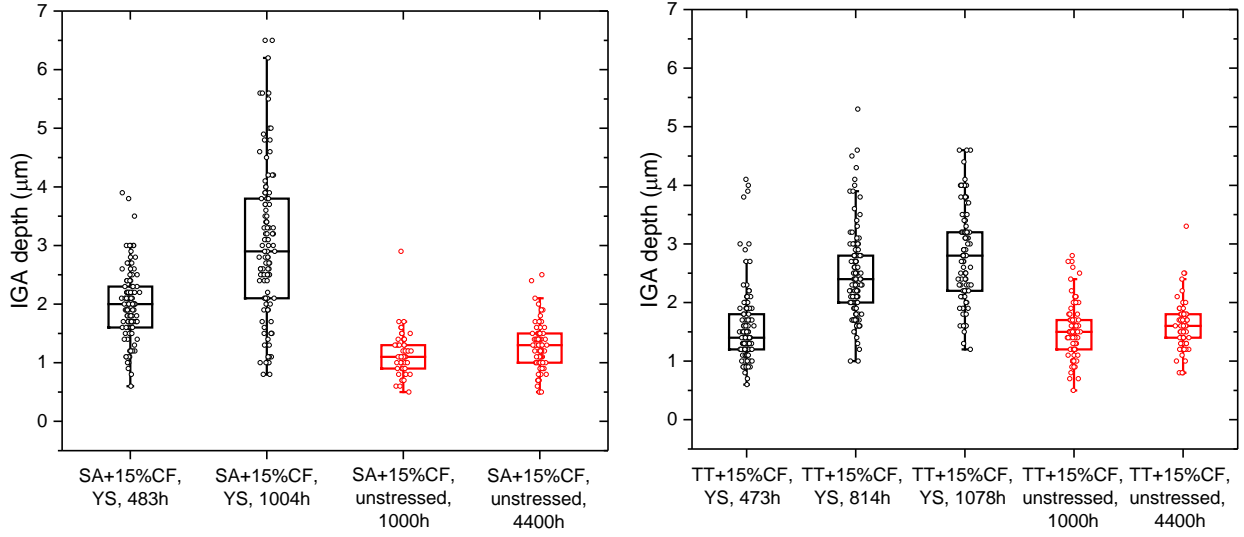


Figure 23. The box and whisker plot of the IGA depth distribution in the Alloy 600 (a) SA+15%CF and (b) TT+15%CF materials with SCC initiation specimens (black) and unstressed exposure coupons (red). The box represents the inner two quartiles of the distribution and the central line represents the median value.

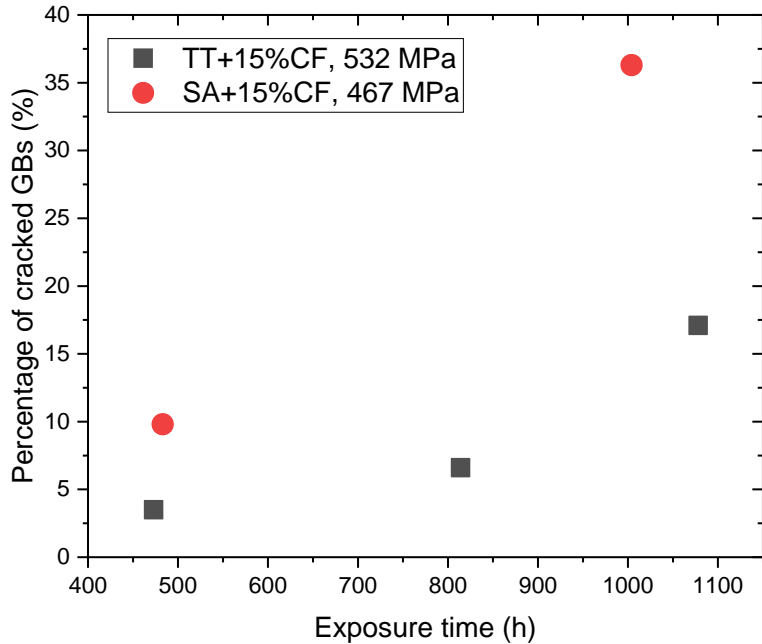


Figure 24. Percentage of cracked grain boundaries observed in the SA+15%CF and TT + 15%CF Alloy 600 SCC initiation specimens after exposure in 360°C PWR primary water. For each specimen, ~110 randomly selected high-energy GBs were measured.

### *Characterizations of SCC Initiation Morphology*

The characterization of SCC initiation morphology is performed on the constant load SCC initiation specimens after test interruptions and at the conclusion of the test, with a focus on the specimens in which SCC initiation was detected by DCPD. A summary of conditions of all the tested SCC initiation specimens is provided in Table 4. The DCPD-measured response during the entire test was also shown in Figure 25 for the SA+15%CF specimens and in Figure 26 for the TT+15%CF specimens, respectively. Among the six specimens tested in the TT+15%CF condition, IN278 was removed before detection of SCC initiation for precursor damage examination, the remaining five specimens exhibited SCC initiation times between 550-960 hours. Similarly, one SA+15%CF specimen (IN282) was removed at ~480 hours (similar to the test duration of that of IN278) to examine precursor damage while the test continued until SCC initiation was detected by DCPD in all remaining specimens between 800-1170 hours. A summary of SCC initiation time as a function of applied stress is also provided in Figure 27 where the macroscopic SCC initiation response of the SA+, TT+, and MA+15%CF Alloy 600 heat NX6106XK-11 specimens are highlighted. The observation of slightly longer initiation times for the SA specimens than the TT specimens is surprising considering the expected beneficial effect of GB carbides in the TT material. However, it is important to note that the TT+15%CF material exhibited a higher yield stress (~532 MPa) versus the SA+15%CF material (~468 MPa). As a result, the applied stress for the TT+15%CF specimens was ~14% higher than for the SA+15%CF specimens.

Table 4. Summary of specimens, material conditions and SCC initiation response for the Alloy 600 heat NX6106XK-11.

Spec. ID	Material Condition	Surface Finish	Applied Stress (MPa)	Time to SCC Initiation (h)
IN273	TT + 15%CF	1 μm	533	957
IN274	TT + 15%CF	1 μm	533	820
IN275	TT + 15%CF	1 μm	530	550
IN276	TT + 15%CF	1 μm	532	817
IN277	TT + 15%CF	1 μm	532	670
IN278	TT + 15%CF	1 μm	530	NI (473)*
IN282	SA + 15%CF	1 μm	466	NI (483)*
IN283	SA + 15%CF	1 μm	467	1132
IN284	SA + 15%CF	1 μm	467	842
IN285	SA + 15%CF	1 μm	468	1170
IN286	SA + 15%CF	1 μm	467	912
IN287	SA + 15%CF	1 μm	473	801

\* NI = no initiation, specimen was removed before DCPD detection of SCC initiation for precursor damage examination.

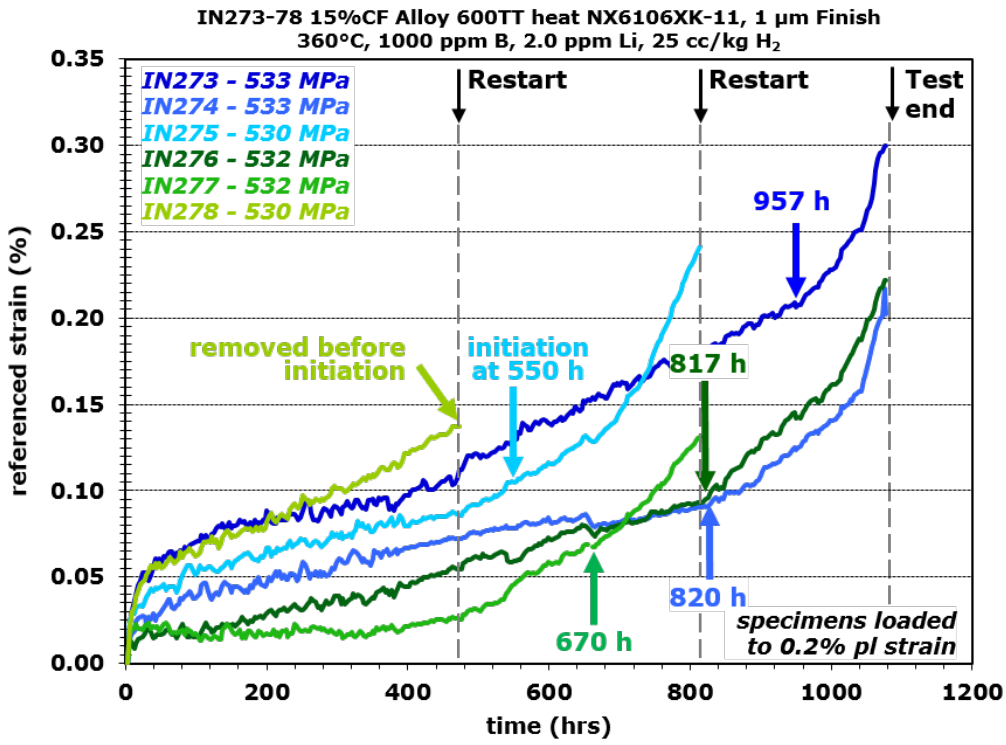


Figure 25. Overall referenced DCPD strain response for the 15%CF Alloy 600TT heat NX6106XK-11 specimens tested at yield stress in 360°C simulated PWR primary water.

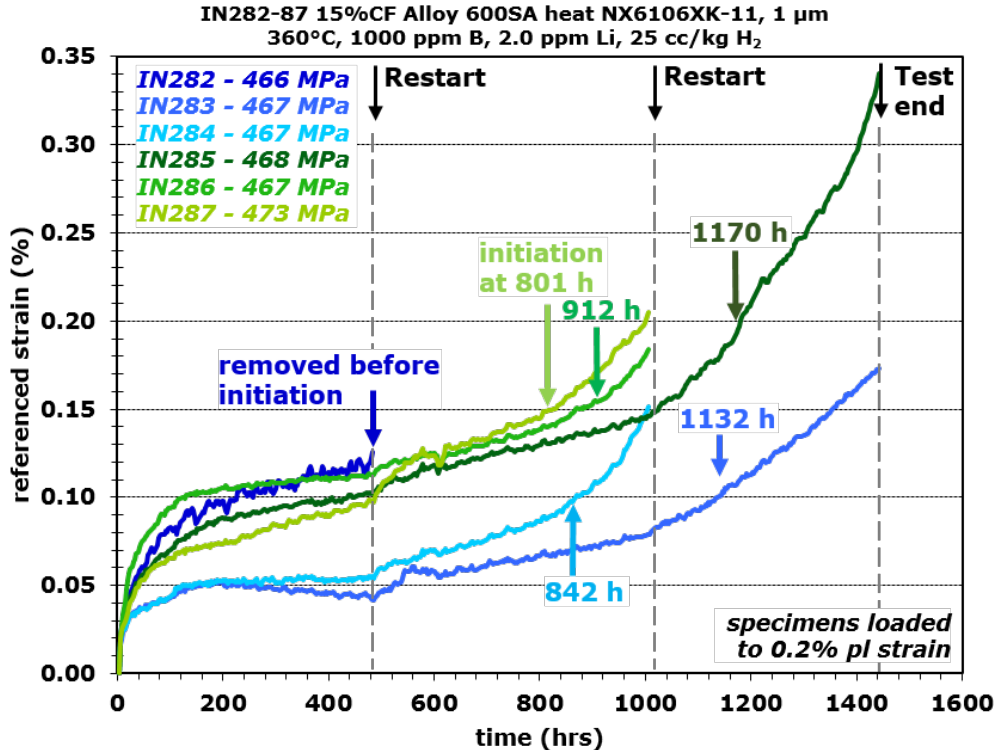


Figure 26. Overall referenced DCPD strain response for the 15%CF Alloy 600SA heat NX6106XK-11 specimens tested at yield stress in 360°C simulated PWR primary water.

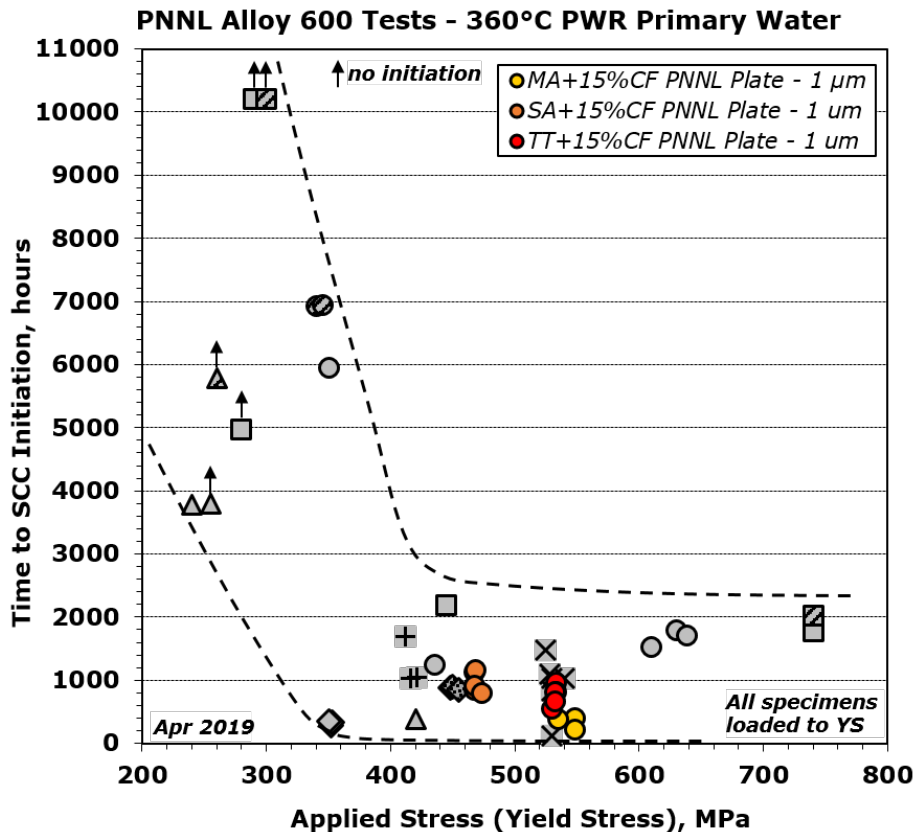


Figure 27. Measured SCC initiation time as a function of applied stress for all tested Alloy 600 specimens. The 15%CF Alloy 600MA, SA, and TT NX6106XK-11 specimens are highlighted.

SEM examinations were performed on all specimens at test interruptions and after DCPD detection of crack initiation with examples shown for the TT+15%CF material in Figures 28-31 and for the SA+15%CF material in Figures 32-34. Obvious cracks are highlighted in red in the SEM-BSE montage images of specimen gauge surfaces. Consistent with the measured SCC initiation times, no significant difference was observed in crack density for the TT and SA specimens. It is also interesting to note that the surface morphology of these TT+15%CF and SA+15%CF specimens upon SCC initiation is very different from that of the same material tested in the MA+15%CF condition. As already reported previously [1, 2, 7], the 15%CF Alloy 600MA specimens exhibited a low density of cracks with one or two extending much longer on the surface than the others, indicative of their dominant role in triggering DCPD detection of SCC initiation. In contrast, a common observation in the TT+15%CF and SA+15%CF Alloy 600 specimens is that several small cracks have initiated at the first interruption around ~480 hours (Figures 29, 30, 32 and 34) but the density gradually increased with test time. In some specimens, cracks can be found all over the gauge surface by the time SCC initiation was detected by DCPD. However, most of the cracks were relatively short, extending to no more than 1-2 grains, making it difficult to attribute SCC initiation to a single, fast-growing crack. Instead, the DCPD detection of crack initiation may be induced by the reduction in cross-sectional area of the gauge due to accelerated growth of multiple short cracks. Supportive evidence can also be found in the specimens removed from the test before SCC initiation was detected. As shown in Figure 28, a crack with a surface length of ~200 um and a depth of 300 um was observed in the TT+15%CF specimen IN278 after 473 hours of exposure. Our previous

study [2] on cold-worked MA specimens suggested that cracks of this size should be able to grow at sufficiently high rates that can trigger DCPD detection of SCC initiation, but SCC initiation was not detected in this specimen by the time it was removed and cross-sectioned. While this crack may have grown at a relatively rapid rate which is indicated by the higher referenced strain in Figure 25, its growth rate was still not fast enough to discern itself from creep as no obvious upturn was detected in the referenced strain.

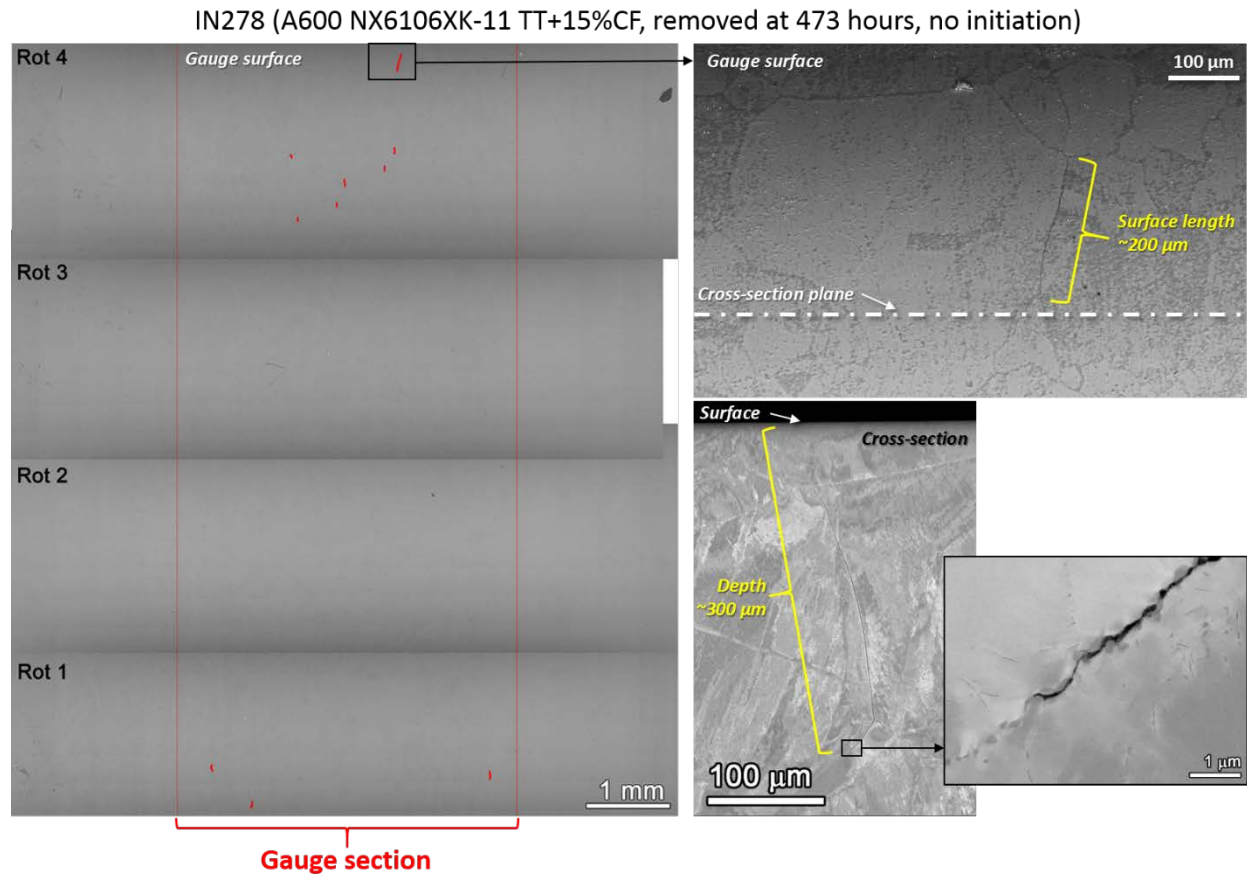


Figure 28. Post-test SEM examination of the 15%CF Alloy 600TT heat NX6106XK-11 specimen IN278 after 473 hours of exposure before SCC initiation was detected by DPCD. The surface morphology is shown on the left with obvious cracks highlighted in red. A zoom-in image of the largest crack found on the surface is shown on the upper right corner with its cross-section morphology shown below.

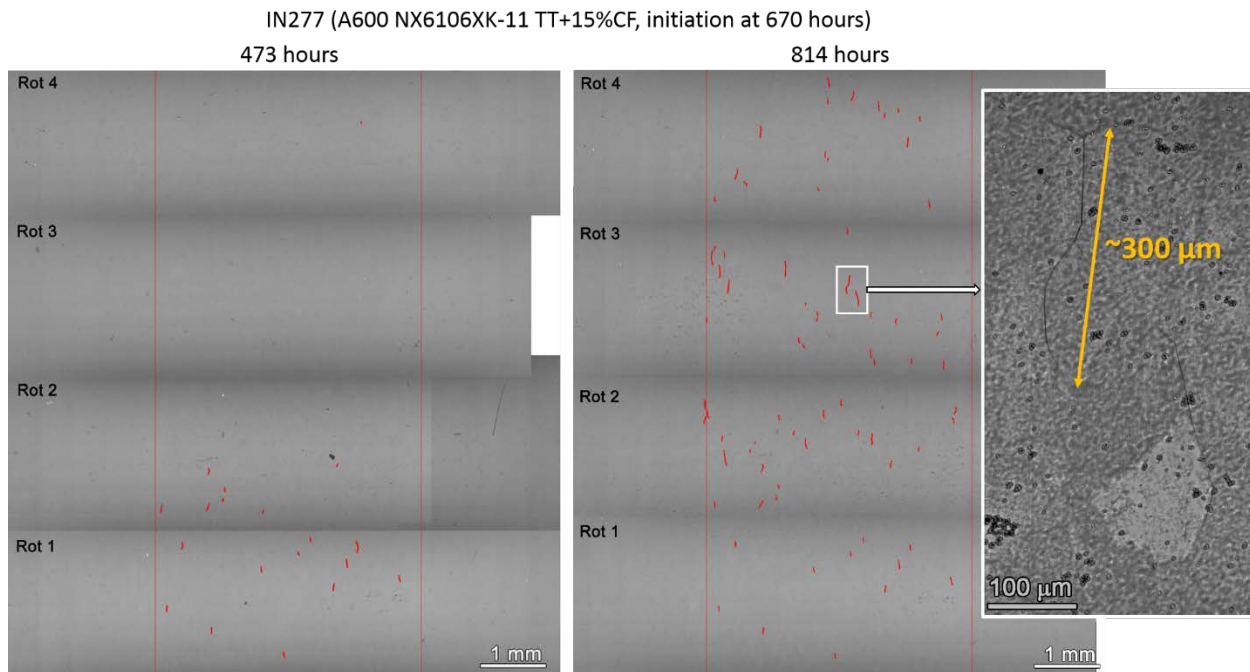


Figure 29. Mid- and post-test SEM examination of the surface of the 15%CF Alloy 600TT heat NX6106XK-11 specimen IN277 in which SCC initiation was detected by DPCD at 670 hours of exposure at yield stress. Obvious cracks are highlighted in red and a zoom-in is provided on the largest crack observed on the surface.

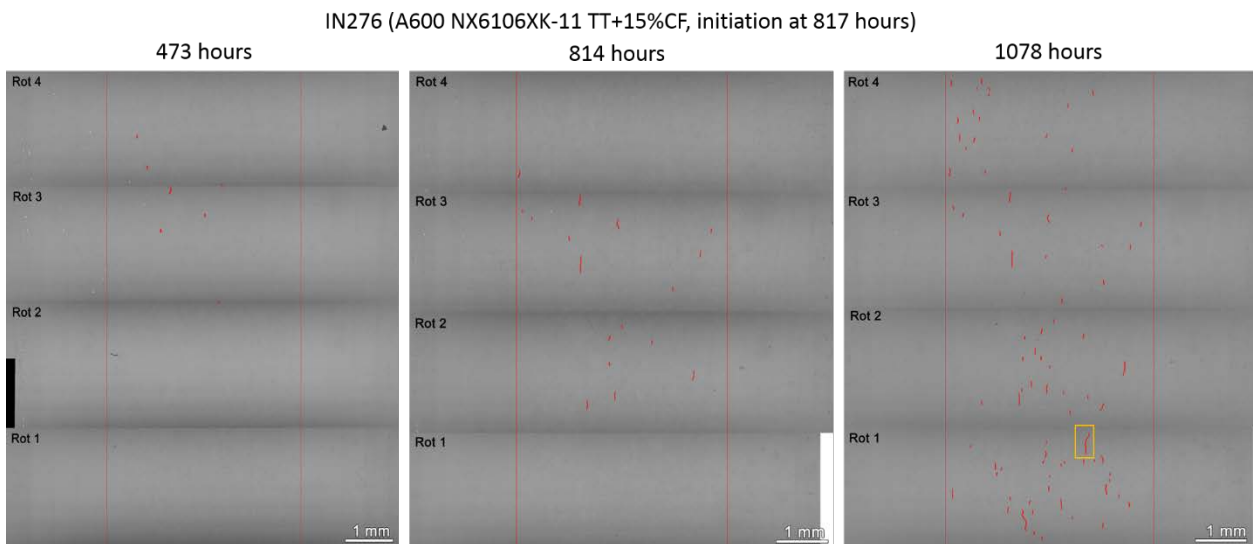


Figure 30. Mid- and post-test SEM examination of the surface of the 15%CF Alloy 600TT heat NX6106XK-11 specimen IN276 in which SCC initiation was detected by DPCD at 817 hours of exposure at yield stress. Obvious cracks are highlighted in red.

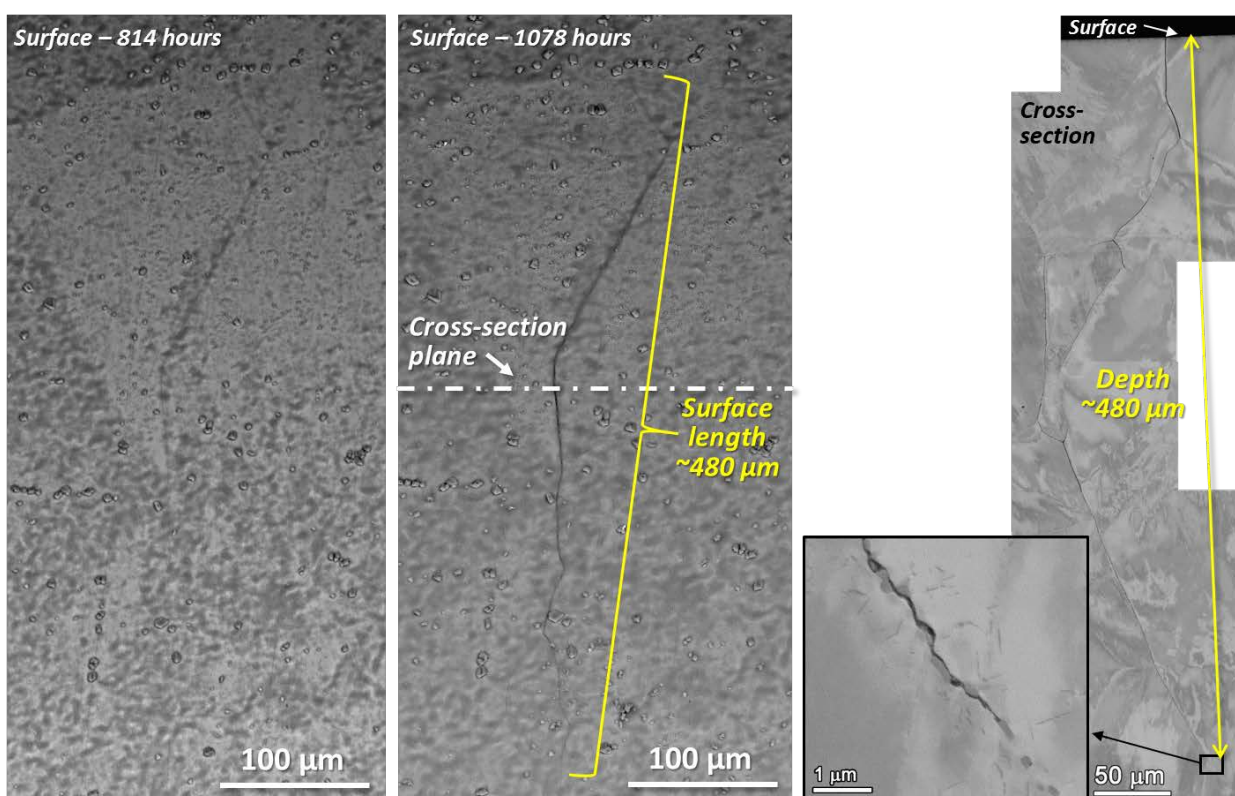


Figure 31. Evolution of the crack highlighted on the surface of IN276 in Figure 30 with its cross-section morphology after 1078 hours of exposure.

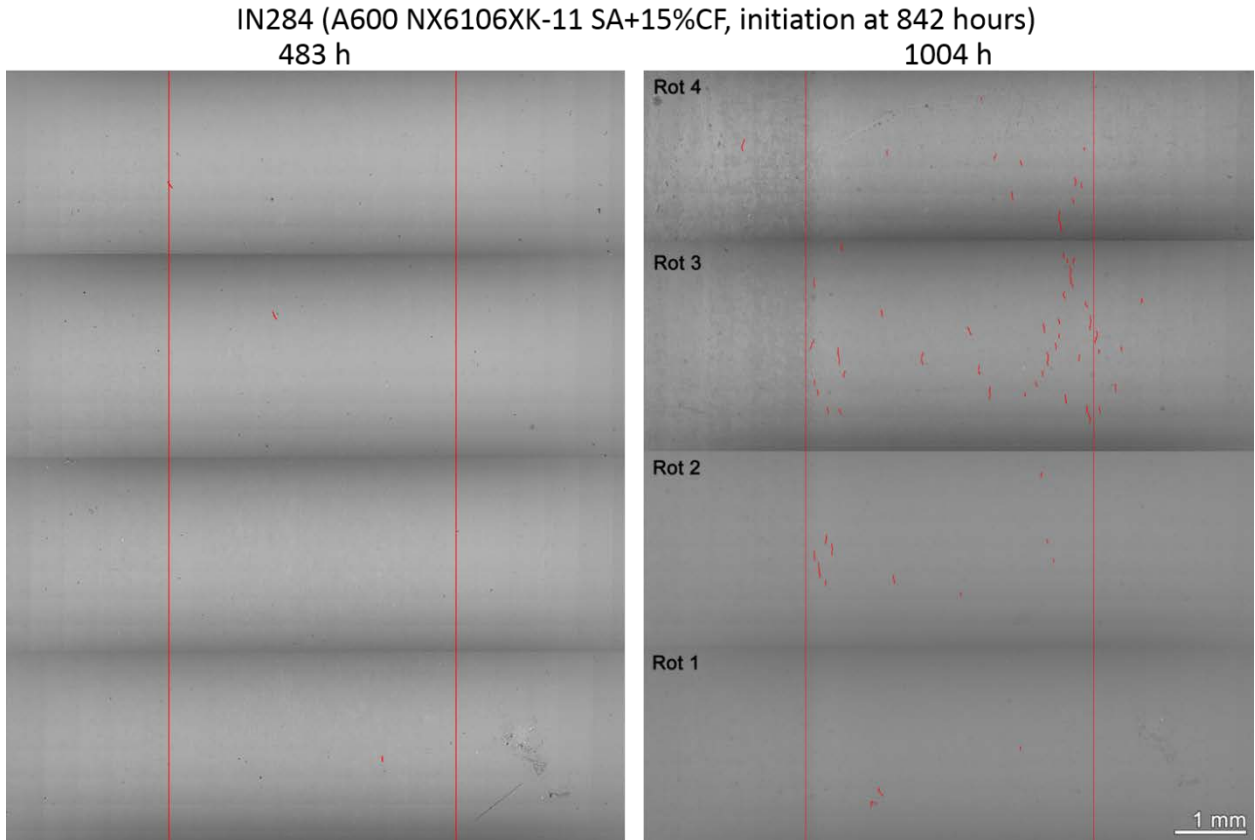


Figure 32. Mid- and post-test SEM examination of the surface of the 15%CF Alloy 600SA heat NX6106XK-11 specimen IN284 in which SCC initiation was detected by DPCD at 842 hours of exposure at yield stress. Obvious cracks are highlighted in red.

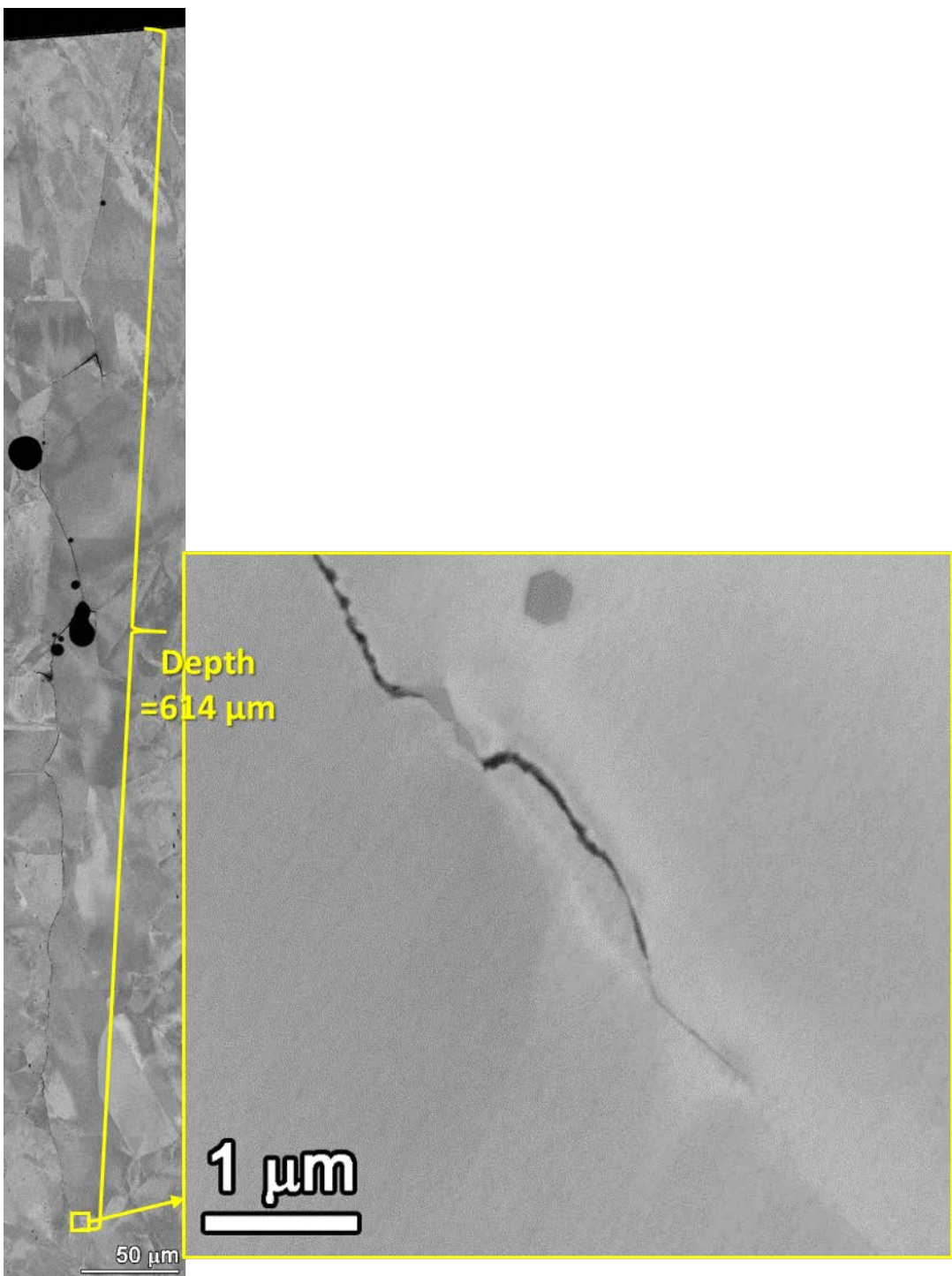


Figure 33. SEM-BSE image of the cross-section morphology of a large crack found in the cross-section of the 15%CF Alloy 600SA heat NX6106XK-11 specimen IN284. The crack tip area is shown at a higher magnification on the right.

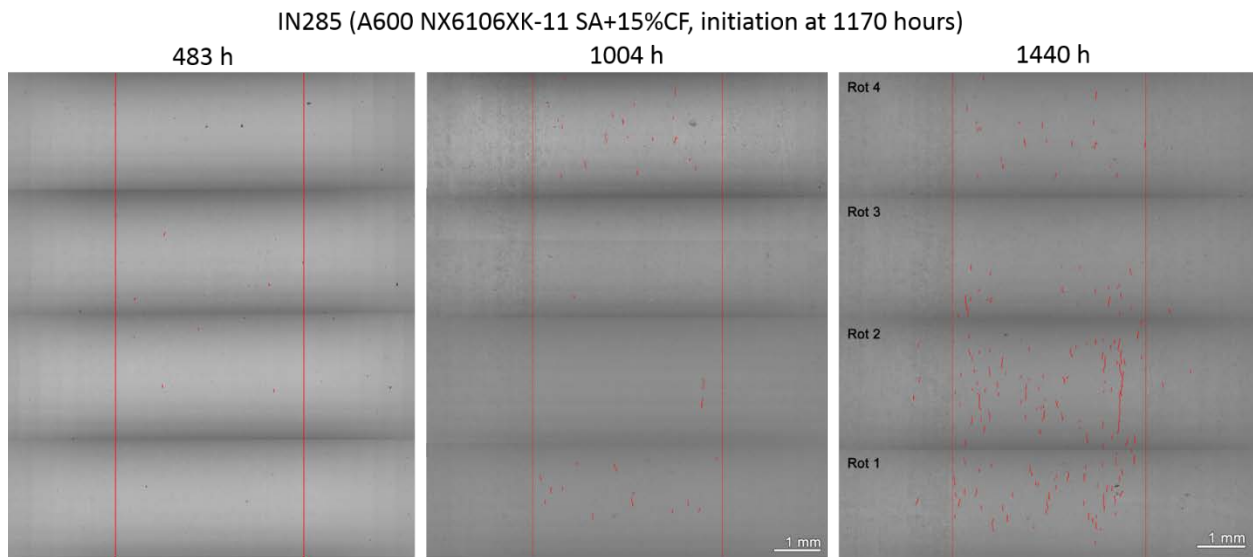


Figure 34. Mid- and post-test SEM examination of the surface of the 15%CF Alloy 600SA heat NX6106XK-11 specimen IN285 in which SCC initiation was detected by DPCD at 1170 hours of exposure at yield stress. Obvious cracks are highlighted in red.

## Discussion

### *Effects of Grain Boundary Carbides on IG Oxidation and SCC Initiation*

The unstressed exposure coupons revealed a slight tendency for the TT condition to exhibit a deeper IGA than their SA and MA counterparts (Figure 12), although boundary-to-boundary variability overlaps with this difference. As discussed elsewhere [6], this slight tendency of the TT material to have a deeper IGA may result from interfacial Cr depletion in a region extending ~400 nm into the matrix on either side of the GB. Interestingly, this trend diminished in the SCC initiation specimens exposed for comparable durations in 360°C PWR primary water. As shown in Figures 22-23, the IGA depths in the SA+15%CF SCC initiation specimens are similar to those in the TT+15%CF SCC initiation specimens after 480 and 1000 hours of exposure. In addition, there is a much higher density of cracked IGA and short IG cracks in the SA+15%CF specimens (Figure 24). However, the similar IGA depth and higher density of short cracks did not seem to have promoted measurable SCC initiation earlier in the SA+15%CF specimens. In fact, SCC initiation was detected within 1000 hours in all five TT+15%CF specimens with the earliest at 550 hours (Figure 25), whereas the first SCC initiation in the SA+15%CF specimen was detected at 800 hours and the last two at around 1150 hours (Figure 26). This makes it difficult to assign a key role of GB carbides in the overall SCC initiation behavior from the current results.

In general, GB carbides are considered to improve SCC resistance in two ways. In the first, the presence of the Cr-rich GB precipitates favors the formation of more protective Cr<sub>2</sub>O<sub>3</sub> that slows IG oxidation/corrosion and SCC [8]. If this is true, deeper IGA should be expected in the SA materials. However, this is not the case in this study as the SA specimens exhibit IGA with a similar depth as those in the TT specimens. Nevertheless, a higher density of cracked IGA and short cracks was observed in the SA+15%CF over the TT+15%CF specimens suggesting an increased cracking susceptibility for the SA material. This was also observed even though the SA+15%CF specimens were loaded at a lower applied stress than the TT+15%CF specimens. TEM examinations [6] on these same material conditions revealed that the oxide aligned with the GB plane in the centerline of the SA material IGA is compositionally distinct with a lower average density or lower Z material than those extends outward to neighboring grains. The TT material IGA exhibited a more complex multiphase oxide with the possible presence of porosity. Nevertheless, it remains unclear whether the compositional difference of the oxides could lead to different degree of porosity and further affect cracking susceptibility.

Alternatively, the GB precipitates mechanically impede crack propagation by blocking/slowing the IG crack propagation [9]. Again, no clear supportive evidence was obtained in this study as most SA+15%CF specimens underwent longer exposure time before the detection of practical SCC initiation in comparison to the TT+15%CF specimens. While this might be partially attributed to a lower applied stress on the SA+15%CF specimens (discussed in the next section), it should be noted that carbon is a potent additional solid solution strengthener and may affect

material creep behavior through interactions with dislocations [10], a process that can occur at relatively low temperature if the stress is sufficiently high, which is relevant to this study. In addition, thermal mechanical treatments can induce alteration of GB chemistry such as segregation of minor element or formation of new phases that may also affect short crack growth behavior. Additional analyses are underway to investigate the GB chemistry and IGA porosity for insights into these differences in behavior.

#### *Effects of Stress on IG Oxidation and SCC Initiation*

As shown in Figure 22, the depth of stress-assisted IGA in the SA/TT+15%CF SCC initiation specimens after ~480 hours of exposure are already deeper than the IGA observed in the unstressed exposure coupons with the same material conditions after 1000 hours of exposure, and continue to grow over time while the IGA in unstressed coupons only exhibit marginal growth. In general, the stress-assisted IGA also appears narrower and more confined along GBs than the unstressed IGA, which is particularly evident in the SA+15%CF materials (Figure 13 vs. Figure 9). This indicates that applied tensile stress has played an important role in the precursor development from very early stage of the test, and that it has affected diffusion process around the leading IGA. This could be a result of plasticity enhanced diffusion as reported by Nguejio et al. [11]. They demonstrated an acceleration of Cr diffusion in Ni single-crystals during a creep test and found a linear dependency between the measured effective diffusion coefficients and the strain rate during secondary creep. It is also worth noting that the growth of IGA depth in the tested specimens appear to be best fitted by a logarithmic equation (Figure 35), coincident with the time dependence of creep at low temperatures [12]. However, the possibility of mass transport through the Cr-rich oxide layer as the rate controlling process cannot be ruled out [13]. In addition, even though a much longer IGA depth was revealed in the SCC initiation specimens over unstressed-coupons, the similar IGA depth observed between the SA+ and TT+15%CF is yet to be explained. More study is needed to elucidate the coupling effects of stress, microstructure, and diffusion on IGA growth.

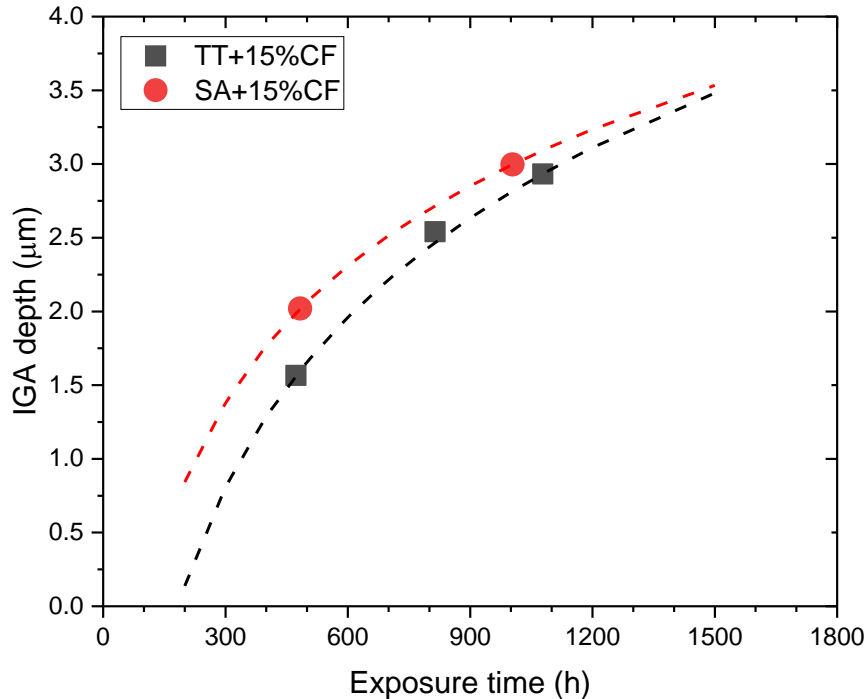


Figure 35. Logarithmic fit of the depth of stress-assisted IGA in the SA+ and TT+15%CF Alloy 600 NX6106XK-11 SCC initiation specimens. The data points are the average IGA depth obtained from measurements on ~110 GBs in each specimen.

Another key aspect for modeling SCC initiation behavior is to define the criteria for the transition of IGA to actively growing cracks, i.e. the cracking of oxidized GBs. In a local IGS SCC engineering model proposed by Couvant et al. [14], they assume that the transition takes place as soon as a critical depth of IGA is reached together with a critical stress to oxide failure. A series of micro-mechanical tests [15, 16] have since been performed along with finite element modeling [17] in search of the critical stress, but so far this hypothesis hasn't been proven by experiment. Although a significant variation may exists in stress at local GBs, the fact that the SA+15%CF SCC initiation specimens loaded at an applied stress ~14% lower than that of the TT+15%CF specimens exhibit a ~2X higher density of cracked GBs after comparable test durations (Figures 22 and 24) suggests that the transition of IGA to cracks cannot depend solely on the magnitude of the applied stress. Instead, creep may have made a significant contribution to this transition by inducing microplastic deformation at the IG oxides and assuming a critical strain exists to fracture the oxide. A preliminary comparison has been made between the percentage of cracked GBs as a function of bulk creep strain in both the SA+ and TT+15%CF specimens as shown in Table 5. For each material condition, the percentage of cracked GB was found to increase with increasing bulk creep strain, supporting the notion of a critical oxide fracture strain. Alternatively, Parkins et al. [12] has demonstrated in constant load tests that a sufficiently fast creep strain rate is necessary for cracking to take place given favorable electrochemical conditions, indicating the effective creep rate the controlling parameter of cracking. From the DCPD-referenced strain response which basically reflects the concurrent

evolution of creep and short crack growth, the SA+15%CF specimens exhibit a higher primary creep component that may have led to a higher density of cracking. Further analysis is needed to validate the use of oxide fracture strain/creep strain rate for modeling the transition from IGA to crack nucleation and growth.

Table 5. Summary of the percentage of cracked GB and uniaxial creep strain measured in cross-sectioned SCC initiation specimens.

<b>Spec. ID</b>	<b>Material Condition</b>	<b>% of cracked GB (%)</b>	<b>Uniaxial creep strain <math>\varepsilon_{cr,L}</math> (%)</b>
IN278	TT + 15%CF	3.5	0
IN277	TT + 15%CF	6.6	0.04
IN276	TT + 15%CF	17.1	0.07
IN282	SA + 15%CF	9.8	0.009
IN284	SA + 15%CF	36.3	1.38

In the short crack growth regime, the effect of stress is difficult to separate from the material condition in this study where the SA+15%CF specimens were loaded at a lower applied stress while the elimination of GB carbides was expected to promote crack growth. However within each single material condition set, the specimen initiated earlier tended to exhibit a higher DCPD referenced strain rate at the “steady” state. This again relates short crack growth to a strain rate expression. SEM examinations are underway to better characterize the contribution of multiple crack nucleation and growth to the referenced DCPD strain response, while additional test and data analysis are being planned to investigate the GB carbide effects on low- $K$  crack growth. Finally, the role of bulk creep behavior needs to be assessed as well as microplastic deformation at leading crack tips in sustaining crack growth (since crack arrest and coalescence is expected for growth of multiple small cracks).

### *Effects of Cold Work*

Cold work has been shown to promote SCC crack growth in Alloy 600, but its role in SCC initiation is less clear. To investigate whether cold work promotes IG oxidation, systematic quantification was carried out on IGA depth in the unstressed coupons after 1000 hours of exposure and a summary plot is provided in Figure 12. Interestingly, data from the SA, SA+TT, and MA conditions all reveal slightly shorter IGA depths in the 15%CF condition in comparison to the non-CW condition. This may be related to the higher density of dislocations produced by cold work acting as reaction sites and paths for enhanced diffusion. This is evidenced in the Alloy 600SA materials as shown in Figures 8 and 9. In the non-CW SA material, the IGAs are generally sharper than those in the SA+15%CF condition. This phenomenon is less prevalent in the TT Alloy 600 materials (Figures 10 and 11), possibly because carbides have deflected the

corrosion/oxidation trajectory around their periphery and obscured the effect of cold work. Nevertheless, the difference observed in the morphology and the depth distribution of IGA between non-CW and CW materials is very small, suggesting moderate cold work alone does not significantly affect IG oxidation behavior in Alloy 600.

### *Implications on Model Development for SCC Initiation*

This study has revealed a predominant role of mechanical effects on the multiscale events leading to macroscopic SCC initiation for the first time, including IGA growth, transition from IGA to crack nucleation and the progression to short crack growth. Clearly, a mechanical component is necessary in modeling SCC initiation behavior of Alloy 600 that is often overlooked in the precursor development stage of IGA growth. In fact, oxidation kinetic models currently available are usually built on data obtained from exposure of unstressed samples in PWR primary water. This can lead to misinterpretation as the synergisms between mechanical, environmental and material factors are neglected. For example, the local model proposed by Couvant et al. [14, 18] does not incorporate mechanical factors but only electrochemical potential and temperature for the estimation of oxidation depth. While a correlation between deformation in creep and precursor damage has been demonstrated in this study, the exact nature of such a correlation is yet to be identified. In particular, the rate-limiting process and criteria of fracture or damage rate needs to be elucidated. Creep strain rate appears to be a promising candidate as the controlling parameter for modeling that can link IGA growth, transition from IGA to crack nucleation, and short crack growth that lead to practical SCC initiation. However, additional experiments and data analyses are necessary relating creep behavior in the bulk and at leading IGA/crack tip with diffusion and fracture mechanics to fully understand these processes and obtain physically-based expressions for SCC initiation. Metallurgical/microstructure factors that can affect creep at relatively low temperatures should also be studied for a comprehensive view of the entire process. Extensive literature review is underway to assess the possibility of integrating/adapting existing models with experimental findings obtained in the current work.

While the above approach is expected to result in mechanistic-based prediction of SCC initiation of individual cracks, stochastic process may need to be incorporated to simulate multiple crack initiation events given the multitude of complexity and randomness involved in the process. If realistic life assessment of components is desired, Monte Carlo simulation may be needed to predict SCC initiation behavior under different scenarios. Although a comprehensive, large scale modeling is beyond the scope of the current project, a framework is under consideration as a proof-of-concept tool to showcase its adaptability with existing larger scale models being used in the industry, such as xLPR.

## **Summary and Conclusions**

Constant load SCC initiation testing has been performed on an Alloy 600 heat in both SA+ and TT+15%CF conditions in simulated PWR primary water with a focus on the effect of material condition and GB carbides on SCC initiation of Alloy 600. Test interruptions were carefully carried out to document precursor damage evolution using detailed microscopy. Depth distribution of IGA and short cracks have been quantified and compared to the data acquired from unstressed coupons of the same material conditions exposed to the same environments. Critical information has been obtained enabling improved mechanistic understanding on the multiple stages leading to practical SCC initiation and underpinning key parameters to model SCC initiation behavior. Although the SCC initiation response of SA and TT Alloy 600 material were expected to exhibit significant differences, the current study has shown only minor differences in the resulting IGA depth and time to practical SCC initiation between these thermal histories. Instead, mechanical factors appear to have a predominant role over GB carbides in both IGA and short crack growth regime, which is likely associated with creep-induced microplastic deformation at leading IGA/cracks. While the microplastic deformation cannot happen without the application of stress, creep/crack-tip strain rate may provide a more rigorous approach to modeling SCC initiation than do stress- or stress intensity-based expressions. In this way, the time-dependence of diffusion processes and microplastic deformation could be incorporated into the model and lead to a better description of the actual SCC initiation processes to which simple considerations of stress cannot achieve. Additional analysis is underway to validate this concept and acquire data inputs necessary for the model development.

## **Acknowledgement**

The authors recognize collaborative research activities funded by the Electric Power Research Institute on the exposure of unstressed Alloy 600 coupons and the Office of Basic Energy Sciences for high-resolution characterizations of GB damage and crack tips. These collaborations have been essential to the success of the SCC initiation research. Critical technical assistance is also recognized from Rob Seffens and Ryan Bouffioux for SCC experimentation and Anthony Guzman for metallographic specimen preparation.

## References

- [1] S. M. Bruemmer, M. J. Olszta, D. K. Schreiber and M. B. Toloczko, *Corrosion and Stress Corrosion Crack Initiation of Cold Worked Alloy 600 and Alloy 690 in PWR Primary Water Environments*. Pacific Northwest National Laboratory: Technical Milestone Report M2LW-13OR0402035, Light Water Reactor Sustainability Program, DOE Office of Nuclear Energy, September 2014.
- [2] Z. Zhai, M. J. Olszta, M. B. Toloczko and S. M. Bruemmer, *Summary of Stress Corrosion Crack Initiation Measurements and Analyses on Alloy 600 and Alloy 690*. Pacific Northwest National Laboratory: Technical Milestone Report M2LW-15OR0402034, Light Water Reactor Sustainability Program, DOE Office of Nuclear Energy, September 2015.
- [3] Z. Zhai, M. B. Toloczko, M. J. Olszta, D. K. Schreiber and S. Bruemmer, *Stress corrosion crack initiation of alloy 600 in simulated PWR primary water*. Pacific Northwest National Laboratory: Technical Milestone Report M2LW-17OR0402034, Light Water Reactor Sustainability Program, DOE Office of Nuclear Energy, September 2017.
- [4] D. Z. Zhai, D. M. Toloczko and D. S. Bruemmer, *Stress corrosion crack initiation behavior of Alloy 600 and Alloy 690 in PWR primary water*. Pacific Northwest National Laboratory: Technical Milestone Report M2LW-18OR0402034, Light Water Reactor Sustainability Program, DOE Office of Nuclear Energy, September 2018.
- [5] D. K. Schreiber, M. J. Olszta, K. Kruska and S. M. Bruemmer, "Role of Grain Boundary Cr<sub>5</sub>B<sub>3</sub> Precipitates on Intergranular Attack in Alloy 600", in *Proceedings of the 18th International Conference on Environmental Degradation of Materials in Nuclear Power Systems – Water Reactors: Volume 1*. 2018, Springer International Publishing, pp. 359-374.
- [6] D. K. Schreiber, M. J. Olszta and D. K. Kruska, *Intergranular oxidation of thermally treated Alloy 600 coupons*. Pacific Northwest National Laboratory: Technical Report DE-AC05-76RL01830, July 2018.
- [7] Z. Zhai, M. B. Toloczko, M. J. Olszta and S. M. Bruemmer, "Stress corrosion crack initiation of alloy 600 in PWR primary water", *Corrosion Science*, Vol.123, 2017, pp. 76-87.
- [8] G. S. Was and K. Lian, "Role of Carbides in Stress Corrosion Cracking Resistance of Alloy 600 and Controlled-Purity Ni-16% Cr-9% Fe in Primary Water at 360°C", *Corrosion*, Vol.54, Iss.9, 1998, pp. 675-688.
- [9] S. M. Bruemmer, L. A. Charlot and C. H. H. Jr., "Microstructure and Microdeformation Effects on IGSCC of Alloy 600 Steam Generator Tubing", *Corrosion*, Vol.44, Iss.11, 1988, pp. 782-788.
- [10] J. Sung, J. W. Jones and G. Was, "Effect of carbon on the low-temperature creep behavior of Ni-16Cr-9Fe", *Metallurgical Transactions A*, Vol.23, Iss.3, 1992, pp. 1033-1037.
- [11] J. Nguejio, J. Crépin, C. Duhamel, F. Gaslain, C. Guerre, F. Jomard and M. Maisonneuve, "Diffusion Processes as Possible Mechanisms for Cr Depletion at SCC Crack Tip", in *Proceedings of the 18th International Conference on Environmental Degradation of Materials in Nuclear Power Systems – Water Reactors: Volume 1*, J. H. Jackson, D. Paraventi and M. Wright, Editors. 2018, Springer International Publishing: Cham, pp. 337-357.

- [12] R. N. Parkins, "1990 Plenary Lecture: Strain Rate Effects in Stress Corrosion Cracking", *Corrosion*, Vol.46, Iss.3, 1990, pp. 178-189.
- [13] A. Machet, "Study of the initial stages of oxidation of stainless steels in high temperature water". 2004, Chimie Physique et Chimie Analytique de Paris Centre.
- [14] T. Couvant, J. Caballero, C. Duhamel, J. Crépin and T. Maeguchi, "Calibration of the Local IGSCC Engineering Model for Alloy 600", in *Proceedings of the 18th International Conference on Environmental Degradation of Materials in Nuclear Power Systems – Water Reactors: Volume 2*, J. H. Jackson, D. Paraventi and M. Wright, Editors. 2018, Springer International Publishing: Cham, pp. 295-317.
- [15] A. Stratulat, D. E. J. Armstrong and S. G. Roberts, "Micro-mechanical measurement of fracture behaviour of individual grain boundaries in Ni alloy 600 exposed to a pressurized water reactor environment", *Corrosion Science*, Vol.104, 2016, pp. 9-16.
- [16] J. Dohr, D. E. J. Armstrong, E. Tarleton, T. Couvant and S. Lozano-Perez, "The influence of surface oxides on the mechanical response of oxidized grain boundaries", *Thin Solid Films*, Vol.632, 2017, pp. 17-22.
- [17] T. Couvant, "Prediction of IGSCC as a Finite Element Modeling Post-analysis", in *Proceedings of the 18th International Conference on Environmental Degradation of Materials in Nuclear Power Systems – Water Reactors: Volume 2*, J. H. Jackson, D. Paraventi and M. Wright, Editors. 2018, Springer International Publishing: Cham, pp. 319-334.
- [18] T. Couvant, M. Wehbi, C. Duhamel, J. Crepin and R. Munier, "Development of a local model to predict IGSCC: preliminary calibration of parameters for nickel alloys exposed to primary water", in 17th International Conference on Environmental Degradation of Materials in Nuclear Power Systems - Water Reactors, August 9-13, 2015, Ottawa, ON, Canada.